Investigating the rheology of fluidized and non-fluidized gas-particle beds – implications for the dynamics of geophysical flows and substrate entrainment

Eric C.P. Breard[1], Luke Fullard[2*], Josef Dufek[1*], Michael Tennenbaum[3,4], Alberto Fernandez-Nieves[3,4], Jean-François Dietiker[5,6].

1: Department of Earth Sciences, University of Oregon, USA
2: School of Food and Advanced Technology, Massey University, New Zealand
3: Department of Condensed Matter Physics, University of Barcelona, 08028 Barcelona, Spain
4: ICREA-Instituci Catalana de Recerca i Estudis Avanats, 08010 Barcelona, Spain
5: National Energy Technology Laboratory, U.S. Department of Energy, Morgantown, WV, USA
6: Leidos Research Support Team, Pittsburgh, PA 15236-0940, USA

*: These authors contributed equally.

Corresponding author:
ebreard@uoregon.edu

Abstract

Natural geophysical mass flows are among the most complex granular systems and their dynamics are often modified by the presence of an interstitial fluid. Prediction of their runout requires the development of models estimating the solid stresses in these hazardous currents wherein excess pore-fluid pressure can develop. We use discrete element modelling (DEM-CFD) with a Coarse-Graining post-processing technique (CG) to investigate the rheology of unsteady gas-particle fluidized to non-fluidized granular beds placed on horizontal and inclined planes. Similar to fluidized beds immersed in viscous fluids, the effective friction coefficient of air-fluidized beds can be defined as a function of the classic *μ(I)-rheology* and the non-dimensional fluid or solid pressure to explain the failure and dynamics of granular flows with excess pore pressure on inclines. However, dilation imposed by fluid drag and particle collisions in gas-particle fluidized beds can drastically change its effective frictional properties. In contrast with the common assumption in water-particle flows that granular temperature is negligible, in our gas-particle simulations, the contribution of the velocity fluctuations to the stress tensor is significant. Hence, the shear stress is found to be non-zero even when the flow is fully fluidized in the inertial regime. These results suggest the need to better understand velocity fluctuations to predict the effective viscosity of

sheared fluidized mixtures and are relevant for many applications. Notably, a unified approach is useful for many geophysical flows that encompass a range of fluidization conditions in a single flow such as pyroclastic density currents and snow avalanches.

1. Introduction

The ability of mobile granular flows to behave like liquids has fascinated scientists for centuries (Coulomb 1781; Reynolds 1885) and has been the focus of studies in physics (Jaeger and Nagel 1992; Pouliquen and Vallance 1999; Jop et al. 2006; Pailha et al. 2008; Boyer et al. 2011; Holyoake and McElwaine 2012), engineering (Beverloo et al. 1961; Langston et al. 1995; Cleary and Sawley 2002; Fullard et al. 2017), soil mechanics (Schoefield and Wroth 1968; Wood 1990), and geology (Calder et al. 2000; Iverson and Vallance 2001; Hutter 2005; Edwards and Gray 2014).. Understanding the rheology of granular matter is essential for modelling systems with particles, but compared to single phase fluids, most constitutive approaches have been developed relatively recently. Difficulties in describing particulate systems originate from their ability to display history- and preparation-dependent strengthening and dilation (Wood 1991; Roux and Radjai 1998), anisotropy and normal stress differences (Weinhart et al. 2013), nonlocality (Aranson and Tsimring 2002; Kamrin and Koval 2012; Henann and Kamrin 2013; Zhang and Kamrin 2017), negligible thermal fluctuations, highly dissipative interactions, and a lack of separation between the microscopic grain scale and the macroscopic scale of the flow (Forterre and Pouliquen 2008). While many flows of granular media in industry can be treated as "dry" media where fluid drag can be neglected, in geophysical mass flows, particles are often fine enough to allow pore-fluid pressure to be generated and sustained for long durations (Iverson et al. 2010; Roche 2012; Lube et al. 2019). The latter case is a form of fluidization; elevated pore pressure forces a "static" solid-like granular system to behave as a liquid by having a fluid percolating through the porous media and applying a drag force opposing gravity (Geldart 1973; Kunii and Levespiel 1991; Grace 1992). With increasing superficial velocity of the fluid, the pore pressure in the bed increases up to the extent where it equals the lithostatic pressure, and the bed is thus fully fluidized. In engineering settings, fluidization is often forced by injecting a fluid near the bed and is generally used because it enhances heat transfer between the fluid and the solid (Mickley and Fairbanks 1955; Chen et al. 2005), which improves reaction rate efficiency. Additionally, mixing of a solid mixture is much easier when fluidized. Industrial fluidization is usually generated in confined systems such as

cylinders or reactors. In geological settings fluidization is much more likely to occur in settings where the material is on a slope and can flow without being constrained by solid boundaries in two dimensions (Roche et al. 2016). Typically fluidization occurs when fluid drag from escaping water or air is imposed upon the solid granular phase; This can occur, for example, as the bed compacts (Sparks 1976; Iverson and Lahusen 1989; Druitt et al. 2007; Girolami et al. 2007; Iverson et al. 2010; Breard et al. 2019), which occurs in debris flows and dense pyroclastic density currents. These two types of flows share many similarities. For instance, their rheology spans that of dry granular to fluidized beds and their long runout is due to the development of the pore pressure feedback (Iverson 2005; Lube et al. 2020). Yet, because the interstitial fluid in debris flows is usually made of muddy water and pyroclastic density currents of hot air, the scaling of the granular rheology differs. The rheology is dominated by the viscous number for debris flows and by the inertial number in pyroclastic density currents (Lube et al. 2020). In addition, the mass loading of ~2 (density ratio of solid over fluid) and high viscosity of the fluid in debris flows influence the solid-fluid coupling. For instance, the lubrication force is expected to be more important in viscous liquids and affects particle interactions, the flow rheology and the solid velocity fluctuations (Ness and Sun 2015).

Advances in granular physics through experiments and numerical simulations (da Cruz et al. 2005; Jop et al. 2006; Forterre and Pouliquen 2008; Fall et al. 2015) have shed light on the mechanics of granular flows. These studies show that in flows where viscous forces are negligible (Stokes number >>1), shear stress and normal stress are correlated with a coefficient of proportionality that is the function of a single non-dimensional parameter known as the inertial number *I*.

$$\sigma = \mu(I)\, P \quad \text{and} \quad I = \frac{\dot{\gamma} d}{\sqrt{\frac{P_s}{\rho_s}}} \qquad \text{(Eq. 1) (da Cruz et al. 2005)}$$

Here μ is the friction coefficient, I describes the ratio of (a) a microscopic timescale $d/(P_s/\rho_s)^{0.5}$, which represents the time it takes for a particle to fall in an open space of diameter d under the pressure P_s, known as the typical time scale of rearrangement, and (b) a macroscopic time scale $1/\dot{\gamma}$ related to the average deformation. Three granular regimes have been defined based upon the scaling of the shears stress with the shear rate and the value of the inertial number. Eq.19

When the granular flow experiences homogeneous shear, the *μ(I)-rheology* (Eq.2) approximates its mechanics and this rheology is local.

$$\mu(I) = \mu_1 + \frac{\mu_2 - \mu_1}{1 + \frac{I_0}{I}} \qquad \text{(Jop et al. 2005; Jop et al. 2006) (Eq.2)}$$

where μ_1 is the static friction coefficient, and I_0 and μ_2 are material constants.

Our aim is to understand how the presence of excess pore pressure modifies the internal strength of a gas-particle granular mixture and reduces its effective viscosity. We focus on granular beds on slopes since these settings are relevant to geophysical mass flows. The novelty of our work lies in the focus on gas-particle flows with excess pore pressure in a transient state using 3D DEM-CFD simulations (i.e. partially to fully fluidized beds) whereas most of the work done on granular flows with excess pore pressure focuses on granular flows immersed in viscous fluids (e.g. water or muddy water which are dominated by viscous forces), and were investigated using experiments or two-layers depth-averaged (2D) methods (Forterre and Pouliquen 2008; Iverson and George 2014; Bouchut et al. 2016).

In this paper, we use the word fluidized to describe a particulate bed with a pore pressure exceeding ambient fluid pressure (e.g. equal to atmospheric pressure in the case of flows in air) and generates fluid flow drag that opposes gravitational forces on the grains. Surprisingly, little quantitative work has been done on the rheology of sheared gas-particle fluidized beds (Roche 2012; Smith et al. 2018), although they are extremely relevant analogs for hazardous mass flows that can move rapidly downslope. Recently, continuum modelling of fully fluidized gas-particle beds using a modified Kinetic Theory (KT) has shown good agreement with experiments (Jessop et al. 2017). However, the KT suffers from limitations near the close packing limit (Chialvo and Sundaresan 2013), which can overpredict the runout of unsteady flows (Breard et al. 2019) and has yet to be adapted to describe transient fluidized to non-fluidized granular flows. Without an understanding of the rheology of fluidized granular flows, modeling flows such as concentrated pyroclastic currents is limited and requires using simplified rheologies (Gueugneau et al. 2017). Even dynamics of static fluidized beds are not trivial, for instance, experimental investigations of fluidized bed viscosity shed lights on the complexity of these system, which do not behave as pseudo-fluids (Gibilaro et al. 2007).

The low permeability of pyroclastic flows implies pore pressure diffusion timescales that are long enough that the drag force and associated low effective viscosity operates on the mass flows for a significant fraction of their transport (Breard et al. 2019). However, since pore pressure cannot be sustained indefinitely, natural mixtures that develop pore pressure will span a whole range of behavior from fully fluidized, partially fluidized, and non-fluidized. Therefore, this study investigates the rheology of fluidized and non-fluidized beds in the framework of the *$\mu(I)$-rheology*. We explore a wide range of bulk behavior expected in the basal avalanche of natural pyroclastic density currents and other fluidized geophysical currents. We devote the study to the use of DEM-

Eulerian in 3D, where the solid phase was monodisperse or slightly polydisperse and the fluid chosen to be air. The rheology is investigated numerically using a Coarse-Graining code to compute continuum fields of solid concentration, shear stress, pressure, granular temperature and shear rate.

In section 3.1, we first illustrate the physical properties of a granular flow that is progressively fluidized in two contrasting settings: on a horizontal plane (i.e. confined) and on an inclined plane (i.e. unconfined), where shear can develop. Thereafter, in section 3.2 we compare the scaling of the friction and solid concentration with the inertial number for fluidized and non-fluidized beds. In section 4.1, we show the shear stress in fluidized beds can be defined as a function of the *μ-rheology* and the effective normal stress. In section 4.2, we illustrate how such definition of effective friction helps predict the behavior (acceleration, steady speed, deceleration) of a bed with excess pore pressure on a slope. In section 4.3, we briefly discuss the depth-averaged approach and the relevance of our findings to the development of two-phase depth-averaged models of gas-particle flows. In section 4.4, we combine the suspension and granular rheologies to describe the viscosity of fluidized beds. Finally in section 4.5, we discuss the occurrence of granular flows with elevated pore pressure in natural settings and their ability to erode their substrate.

2. Methods

2.1 Discrete Element Method

In an attempt to gain insights into the relationship between rheology and the granular structure of non-fluidized and fluidized beds we model particles with the Discrete Element Method (DEM). DEM simulations are performed with the MFIX open-source code developed by the US Department Energy's National Energy Technology Laboratory (NETL). Using this method, individual particle-particle and particle-wall interactions can be simulated. Collisional and frictional contacts between particles were modeled with the soft-sphere approach using the spring-dashpot approach (Garg et al. 2012; Li et al. 2012). The mixture is represented by N_m Lagrangian spheres of diameter, D_m, and solid density, ρ_s. Solving Newton's Laws of motion provides the particle momentum and position:

$$\frac{dX^{(i)}(t)}{dt} = V^{(i)}(t) \quad \text{(Eq.3)}$$

$$m^{(i)}\frac{dV^{(i)}(t)}{dt} = {F_T}^{(i)}(t) = m^{(i)}g + {F_d}^{(i\in k,m)}(t) + {F_c}^{(i)}(t) \quad \text{(Eq.4)}$$

$$I^{(i)}\frac{d\Omega(t)}{dt} = T^{(i)}(t) \quad \text{(Eq.5)}$$

where $X^{(i)}$ is the particle position of the i-th particle within the domain at time t, $V^{(i)}$ is the velocity, Ω is the angular velocity of the i-th particle, $m^{(i)}$is the particle mass. ${F_c}^{(i)}$ is the net contact force, ${F_T}^{(i)}$ is the sum of the forces acting on particle i-th, ${F_d}^{(i\epsilon k,m)}$ is the total (viscous and pressure) drag force acting on particle i, if the m-th solid phase is located within the k-th cell. $T^{(i)}$ is the sum of the all torques acting on the i-th particle and $I^{(i)}$ is the moment of inertia.

In the soft-sphere approach, the overlap between particles is represented by series of springs and dashpots in both tangential and normal directions. The loss of kinetic energy during inelastic collisions is modeled with the dashpot, whereas the spring models the stiffness of the solid particle-particle contact.

The coupling between the particles and the Eulerian fluid is described by the transfer of momentum between phases ($\overrightarrow{I_f}$), which is achieved via summing the drag force and pressure gradient force of particles located in the computational cell [*Garg et al.*, 2012]:

$$\overrightarrow{I_f}(t) = \frac{1}{v_{REV}}\sum_{k=1}^{N_k}\overrightarrow{F_D}^{(k)}(t)K_{REV}\left(X_p^{(k)}\right) \quad \text{(Eq.6)}$$

Where $K_{REV}\left(X_p^{(k)}\right)$ is a generic kernel with compact support that determines the influence of the particle force at $X_p^{(k)}$ on the representative elementary volume v_{REV} of the kth grid cell. In the first stage, the algorithm sums the weighted contribution of the particles in each cell. The second stage uses the compact support kernel to interpolate the particles properties at the fluid node as a function of the sum in the neighboring cells computed during the first stage.

The drag force $\overrightarrow{F_D}^{(k)}$ of the particle residing in the cell *k* is defined as [*Garg et al.*, 2012]:

$$\overrightarrow{F_D}^{(k)}(t) = -\nabla P_f(t)\left(\frac{\pi}{6}\,{d_p^{(k)}}^3\right) + \frac{\beta_{fs}^{(k)}(t)}{\left(1-\varepsilon_f(t)\right)}\left(\frac{\pi}{6}\,{d_p^{(k)}}^3\right)\left(\overrightarrow{v_f}(t) - \overrightarrow{v_p}^{(k)}(t)\right) \quad \text{(Eq.7)}$$

Where P_f is the fluid pressure, d_p is the particle diameter, ε_f is the volume fraction of fluid, v_f and v_p are the fluid and particle velocity, respectively. To calculate the drag force accurately, the mean fluid-phase velocity is interpolated to the particle location. Then, the drag force on each particle is

projected on the Eulerian fluid phase grid. The interphase momentum exchange term $\beta_{fs}^{(k)}$ is evaluated via a drag model following Gidaspow (1994):

$$\beta_{fs}^{(k)}(t) = \begin{cases} \frac{3}{4} C_D^{(k)}(t) \frac{\rho_f \varepsilon_f(t)(1-\varepsilon_f) \left\| \overrightarrow{v_f} - \overrightarrow{v_s}^{(k)} \right\|}{d_p^{(k)}} \varepsilon_f{}^{-2.65}, & \varepsilon_f \geq 0.8 \\ \frac{150\,(1-\varepsilon_f(t))^2 \eta_f}{\varepsilon_f(t)\, d_p^{(k)2}} + \frac{1.75\,\rho_f (1-\varepsilon_f(t)) \left\| \overrightarrow{v_f}(t) - \overrightarrow{v_s}^{(k)}(t) \right\|}{d_p^{(k)}} & \varepsilon_f < 0.8 \end{cases} \quad \text{(Eq.8)}$$

with ρ_f as the fluid density. The drag coefficient $C_D^{(k)}$ is calculated as follows (*Gidaspow* 1994):

$$C_D^{(k)}(t) = \begin{cases} \frac{24}{Re^{(k)}(t)\left(1+0.15\,Re^{(k)}(t)^{0.687}\right)} & Re^{(k)}(t) < 1000 \\ 0.44 & Re^{(k)}(t) \geq 1000 \end{cases} \quad \text{(Eq.9)}$$

The full equations of the DEM-CFD code have been added to a supplementary tables S1 and S2. Variations of the form of the Gidaspow drag law described with a sharp or smooth transition around a voidage ε_f=0.2 does not influence our results and their interpretation (Fig. S1).

The MFIX-DEM approach has been rigorously verified in a series of studies that span monodiperse and polydisperse grain-size distributions in wall bounded flows and fluidized/spouted beds (Garg et al. 2012; Li et al. 2012; Musser et al. 2021). More information regarding the physics involved in the DEM model is provided in Garg et al. (2012).

In order to assess whether lubrication forces are important, we use the scaling analysis of Carrara et al. (2019), which states lubrication forces are important in a granular media solely if the following two conditions are fulfilled:

$$log_{10}\left(\frac{Av_p}{U_T}\right) > 0 \; and \; log_{10}\left(\frac{Av_p}{U_T}\right) / \, log_{10}\left(\frac{v_f}{2aU_T}\right) > 1 \quad \text{(Eq.10)}$$

Where A expresses the relationship between the normal and tangential lubrication forces (Marzougui et al. 2015), U_T is the terminal fall velocity of the particles, v_p is the relative velocity between particles, v_f is the relative velocity between fluid and particles and a is the permeability parameter (Bergantz et al. 2017). In our simulations, $log_{10}\left(\frac{Av_p}{U_T}\right) < -3$ and $log_{10}\left(\frac{Av_p}{U_T}\right) /$

$log_{10}\left(\frac{v_f}{2aU_T}\right) < 0.4$. Hence, all our simulations fall within the buoyancy domain as defined by Carrara et al. (2019), where lubrication forces are unimportant. Similarly, lubrication forces are expected to be negligible in gas-particle flows and are therefore excluded from our investigation.

We chose to simulate particles of 0.005m in diameter d with a density of 2500 kg.m^{-3}. Between 4799 and 9508 particles were used with a particle-particle and particle-wall friction coefficients both set to a value of 0.5. The particle stiffness coefficients (k_n and k_t) were chosen as 5x10^4 Pa.m, well above the minimum required to ensure hard collisions for the pressure investigated. Based upon these physical properties, we simulate experiments to determine the angle of repose of the mixture, by imposing a periodic boundary in the spanwise direction and a domain depth equivalent to 20 particles diameter. Fig.1b shows the 3D collapse of the mixture that came to rest with a mean surface angle of 18.5°. Its tangent gives the static friction coefficient of 0.364.

As we investigate both non-fluidized and fluidized bed rheologies from DEM simulations, we perform DEM-Eulerian modeling, with the Eulerian phase chosen as air at an ambient temperature of 293.15 Kelvin and obeying the ideal gas relation (molecular weight of 28.97 g/mol). The 3D Eulerian grid spacing was chosen as 2 particle diameters in all dimensions ensuring accurate gas-particle coupling. The upper domain boundary was set as a pressure outflow with a constant set pressure of 1.0132x10^5 Pa and the gas viscosity was calculated from the Sutherland law (Sutherland 1893). The mixture is gas fluidized by the use of a basal mass-inflow boundary where air at ambient temperature was injected at a controlled superficial upward velocity. In a series of 16 3D DEM-Eulerian static simulations, where both X and Z dimensions had periodic boundaries (ensuring no wall effect) we measured the gas pore pressure at the base of the column (in the lowermost cell that did not contain the static rough layer). The superficial gas velocity is plotted against the pore pressure (Fig.1c), and shows that the minimum superficial velocity *Vs* of 1.85 m/s yields minimum fluidization, while bubbling occurs at a superficial velocity *Vs* exceeding ~2.0 m/s. In order to study the rheology of fluidized and non-fluidized beds, we use a variety of DEM-CFD simulations that are summarized below. The investigation required a set of simulations where we changed individually the boundary parameters: confined or unconfined, gas-fluidized or non-fluidized and the initial conditions of the setup: on a slope, with or without a confining pressure and with or without a rough erodible bed.

Each set of numerical experiments focused on a distinct portion of the fluidized/non-fluidized parameter space and is presented in the order of their appearance in figures.

Fluidized bed

Type 1.1: Confined

In this simulation we modelled the progressive fluidization (increase at rate of 0.2 m/s^{-2}) of a bed confined by periodic boundaries and on a horizontal plane. A rough base of 361 particles of 0.005m diameter was implemented in the model and made static at all times. 8747 particles were initially distributed in a 3D lattice with an initial, isotropic, granular temperature ensuring 'random' collisions during collapse.

Type 1.2: Destabilization by fluidization on a slope

We used this technique to recover the $\mu(I)$-rheology and $\Phi(I)$ of fluidized beds by setting the slope constant and changing the superficial velocity over time (0.04 m/s per sec). This type of simulation was used to understand the scaling between the dimensionless pore pressure and the dimensionless solid pressure. Sensitivity testes indicate the results are independent of the value of superficial gas acceleration chosen (Fig. S2).

Non-fluidized bed

Type 2.1: Destabilization of beds with free-surface

This setup technique was used to recover the $\mu(I)$-rheology and $\Phi(I)$ of non-fluidized granular beds. We modelled the slow destabilization of a bed of 4419 particles by rotating gravity over time (simulating increasing inclination of the bed), at a slow rate of $\frac{0.2\pi}{180}$ $rad.s^{-1}$, which is half an order of magnitude lower than the relaxation rate of the bed found to be $\sim$1.1 $rad.s^{-1}$ to ensure these are pseudo-steady conditions. The lower boundary was made of particles, forced to be static, and every second row was displaced upward by 0.5 particle diameter, to ensure a no-slip boundary condition. We separately varied the contact stiffness and restitution coefficient in order to assess their effect on the flow rheology across the quasistatic, intermediate and inertial regimes.

We also compare the monodisperse mixture of 5 mm spherical particles with a slightly polydisperse size distribution with three size fractions in the following proportions of their diameter: 1/3 of 4 mm, 1/3 of 5 mm and 1/3 of 6 mm.

Type 2.2: Shear cell

In these 200 simulations, we aimed at recovering the $\mu(I)$-rheology and $\Phi(I)$ for a wide range of inertial numbers (10^{-6}–$2x10^{0}$) in a steady state, which allowed us to compare our results with the destabilization simulations (type 2.1). In the setup, the bottom plate was static while the top plate velocity was imposed to shear the bed. The plate could move up and down to keep a constant confining pressure.

Erodible substrate

Type 3: Shear cell with erodible bed

These simulations compared the mobilization of an erodible substrate by a granular flow with and without the effect of pore pressure. A bed of 4799 particles was sheared by setting the rough top plate of 361 particles with a velocity of 5 m/s, and an erodible bed made of 8747 particles was sitting atop a rough static plate of 361 particles. The fluidized case was achieved by having a superficial velocity of 2.0 m/s.

To illustrate in more details the role of granular temperature on the nonlocal behavior of granular flows propagating upon an erodible substrate, we ran 23 shear cell simulations with 35984 particles. The bed was confined between a bottom rough static plate and a top rough plate to which we attributed a velocity from 0.0001 to 100 m/s and a constant pressure of 8 kPa. All particles with a position <0.14m were set with a 0 velocity until the bed of ~0.05m of thickness reached steady state. After 15s, the rough substrate was able to respond to the shear flow above. There was no excess pore fluid pressure in any of the 23 simulations.

Unless stipulated otherwise, the DEM-CFD simulation parameters used are summarized in Table 1. For clarity, we indicated in Table 2 the type of simulation used to generate the data provided by all figures involving the DEM-CFD.

a. Coarse Graining

The coarse graining method (CG) is a computational tool designed to study discrete systems (e.g. DEM-CFD simulations) and built to calculate continuum fields, in particular the stress tensor. The CG method has advantages over other methods in its ability to create fields that satisfy the conservation equations of continuum mechanics even for small numbers of particles, and does not require an assumption of particle shape or stiffness. The sole assumptions are that each contact between two particles is a “point contact” and collisions are not instantaneous. Multiple studies

have successfully involved CG for granular flows in numerical (Thornton et al. 2012; Weinhart et al. 2012; Weinhart et al. 2016), experimental studies (Janda et al. 2015; Rubio-Largo et al. 2015) and even molecular flows (Hartkamp et al. 2012).

Note that the "coarse-graining" term may be ambiguous since it consists in molecular dynamics in replacing an atomistic description with a collection of molecules, and similarly this is applied for DEM of granular flows to describe a continuum of a collection of multiple particles (Queteschiner et al. 2017). In this paper, it is applied to the micro-macro transition method developed in Babic (1997) and extended by Weinhart et al. (2016).

The mixture total stress tensor is simply the sum of the kinetic and contact stress tensors:

$$\sigma(\boldsymbol{r},t) = \sigma^k(\boldsymbol{r},t) + \sigma^c(\boldsymbol{r},t) \quad \text{(Eq.11)}$$

Where the kinetic tensor depends on particle velocity fluctuations and the contact tensor depends on the contact forces. The full description of the tensors is provided in the Supplementary Information.

The granular friction coefficient is calculated from the 2D version of the stress tensor in combination with the pressure using all 3 contributions, which is the best approach for plane shear configuration (Chialvo and Sundaresan 2013; Gallier et al. 2014; Ness and Sun 2015; Weinhart et al. 2016; Zhang and Kamrin 2017).

$$\mu = \frac{|\sigma^D|}{P_s} \quad \text{(Eq.12)}$$

where $|\sigma^D| = \sqrt{0.5\acute{\sigma}^D{}_{ij}\acute{\sigma}^D{}_{ij}}$ (Eq.13). All the data presented in this manuscript are for beds that are yielding (i.e. where a shear rate is measurable).

The average normal stress or solid pressure in the system is calculated as the trace of the 3D stress tensor:

$$P_s = \frac{1}{3}tr(\sigma) \quad \text{(Eq.14)}$$

The granular temperature inside the mixture is defined as:

$$T_g = \frac{tr(\sigma^k)}{3\rho} \quad \text{(Eq.15)}$$

One essential parameter to scale the friction coefficient and solid concentration is the inertial number:

$$I = \frac{\dot{\gamma}\acute{d}}{\sqrt{\frac{P_s}{\rho_s}}} \quad \text{(Eq.16)}$$

where ρ_s is the solid density, $\dot{\gamma}$ is the shear rate, $\acute{d}$ is the mean particle diameter.

For polydisperse systems, the inertial number is calculated with the volumetrically averaged particle diameter $\acute{d}$ known as the D43 (Gu et al. 2016):

$\acute{d} = D_{43} = n_q d_q$ (Eq.17)

Throughout the text, we use the term pore pressure to refer to the differential pore fluid pressure (absolute pore fluid pressure – ambient absolute pressure of the fluid phase).

In this manuscript, the term lithostatic pressure refers to the bed weight per unit area when non-fluidized, which is the depth-integrated normal stress. For instance, a bed with an excess pore pressure of 50%, consists in a bed where the pore pressure/lithostatic pressure = 0.5. When the pore pressure = lithostatic pressure, the bed is fully fluidized.

3. Results

3.1 Numerical rheology

3.1.1 Confined fluidized bed

A detailed and predictive description of the viscosity of granular beds has remained elusive (Grace, 1970; Gibilaro et al., 2007). Measurements are extremely difficult to achieve in practice and if undertaken with a two-stirrer rheometer blade, physical properties such as the solid pressure remain unknown and the shear rate is heterogeneous. Here, we use a CG analysis to calculate the effective viscosity of fluidized beds with air. In the following sections, the rheology of a bed confined and on a horizontal plane is illustrated as it progressively transforms from a non-fluidized media into a fully fluidized and bubbling bed. We then compare the evolution of the same bed undergoing similar transitions (non-fluidized to bubbling) when unconfined (i.e. can flow) and placed on an inclined plane. Next, we confirm that steady and unsteady (i.e. transient) beds display the same rheology. Finally, the similarities between fluidized and non-fluidized granular flow rheologies are demonstrated. Finally, most granular flows simulated are in a transient state where the slope or excess pore pressure changes over time, which is relevant to natural and experimental geophysical applications.

To illustrate the evolution of the rheology of non-fluidized to fully fluidized beds, we run a DEM-CFD simulation where the superficial gas velocity starts at 0 m/s and slowly increased at a rate of 0.2 m/s^{-2}. Data is exported from these simulations every 50 ms for CG analysis. We illustrate the evolution of the bed rheology at various pore-fluid pressures using the CG for the lowermost half

of the bed (0–0.04m above the bottom rough plate). From superficial gas velocity of 0–1.85 m/s, the flow is homogeneously fluidized and no bubbles form. The data shows no fluctuations despite the lack of time-averaging. In the homogeneous stage, the pore pressure increases (Fig.2a) and the solid pressure decreases (Fig.2b) non-linearly as the superficial gas velocity increases. Meanwhile, the solid concentration shows little variation (~1 vol.%) from non-fluidized to the onset of minimum fluidization at $V_s=V_{mf}$ ~ 1.8-1.85 m/s (Fig.2d). At the minimum fluidization, the fractional solid and gas pressure reach 0.1% and 99.9% of the lithostatic pressure. Subsequently, the friction coefficient decreases from the static value of 0.355 to 0.3. The weak dilation the bed experiences (See insert of Fig.2c) is also followed by a reduction of the number of contacts by 4% between $V_s=0$ m/s to $V_s=1.4$ m/s when the friction coefficient is lowest. We illustrated the FrictioMobilization Index (*Im*), which is the ratio $Ft/(Fn\times\mu_{pp})$, where Ft and Fn are the magnitude of the tangential and normal contact force, respectively. μ_{pp} is the particle-particle friction coefficient we used in the DEM code (=0.5). Such a parameter can be useful to understand liquefaction (Guo and Zhao 2013; Yang et al. 2021). At each timestep, a distribution of *Im* for all particle contacts provides a mean of the distribution and number of contacts with *Im*<1, which indicates the yield state of the system since all contacts with *Im*<1 are not sliding (or fully mobilized) (Fig.2e). The distribution between $V_s=0$ m/s, $V_s=1$ m/s and $V_s=1.4$ m/s are relatively similar for *Im*<0.9 (decline of proportion of contacts with increase of *Im*) but the increase in the proportion of contacts with *Im*=1 and near sliding (*Im*>0.9) illustrates the yield of the system despite measuring a friction coefficient below the static friction coefficient of ~0.36. While the bed is dilating and prior to being fully fluidized, there is only partial mobilization of the friction between particles.

When the superficial velocity equals ~1.9 m/s, bubbles form and are accompanied by the large fluctuations in gas and solid pressures, concentration and friction coefficient. Note that the friction coefficient increases drastically from V_{mf} onwards as particle collisions increase. This is also illustrated in the distribution of the Friction Mobilization Index, where ~46% of contacts are sliding. Typically, it is assumed in static fluidization experiments that the pore pressure is a proxy to the solid pressure in the homogeneous phase (Roche et al. 2012). This calculation shows that the pore pressure scales linearly (slope of 1) with the solid pressure except at the low superficial velocities (0–10% of V_{mf}).

In summary, the decline of the friction coefficient (below static friction) prior to bubbling is attributed to the partial mobilization of the friction (sliding) which is induced by the slight dilation of the bed due to the presence of excess pore pressure. The waning of the friction coefficient below

the static friction coefficient is expected only in settings where the bed cannot "flow" to respond to the change of effective stresses because it is confined. Once enough contacts are mobilized (~20%, see Fig.2e), the friction coefficient of the bed exceeds the static friction coefficient.

Most engineering studies focus on static fluidized beds. However, in geological settings, pore-fluid pressure can develop in debris flows or pyroclastic flows that propagate on inclined surfaces and in configurations where the bed is not confined in 2D. Thus, in the next section, we examine the rheology of the fluidized bed on an incline.

3.1.2 Fluidized bed on a slope

Using DEM-CFD, we show how pore pressure evolution modifies the granular bed rheology from dry to fully fluidized, as this whole range of behavior is expected to occur in geophysical flows. Flowing of the mixture is achieved by inclining gravity to mimic a 24° slope. At such an angle, the bed rapidly reaches steady state devoid of pore pressure (<10s) and gas is injected in the lower boundary afterwards. The CG analysis results and pressure data are exported at every 50 ms. Note that the minimum fluidization is reached at superficial velocity of 4.46 m/s. Above this gas velocity, the bed starts bubbling. Noticeably, the onset of bubbling coincides with a sudden change in slopes for all parameters plotted against superficial velocity. The behavior of the fluidized bed is very different from that of the confined bed. While the gas pore-pressure increases and the solid pressure decreases with increasing superficial velocity, the pore pressure reaches the solid lithostatic pressure at V_{mf} (i.e balances the lithostatic pressure) whereas the average solid pressure remains fluctuating around 18% of lithostatic pressure (Fig.3a and 3b). Subsequently, the solid concentration rapidly drops from 58% to reach 20% at V_{mf} (Fig.3c). Meanwhile, the friction coefficient increases systematically (well above the static friction coefficient) with superficial velocity and reaches a plateau around a value of 1.1 in the bubbling regime (Fig.3d).

Fluctuations are higher for all properties than in the confined case (see Fig.2). The non-dimensional pore pressure against the non-dimensional solid pressure falls along the slope of one, up to a non-dimensional solid pressure of 0.4 (Fig.3e). Note that the solid pressure never goes to zero, because particle collisions and velocity fluctuations never vanish.

3.2 $\mu(I)$-rheology and $\Phi(I)$ of pressure balanced and fluidized beds

3.2.1 Instantaneous versus time-averaged rheology of pressure-balanced beds

We investigate the role of pore pressure on the granular bed and how the bed responds to the change of normal stress (alleviated by the formation of pore pressure). We first present results from simulations where the bed is immersed in air with a pore pressure equilibrated to the ambient (without excess pore pressure) and the bed is confined only by its own weight. A similar approach was used in other granular rheology studies but typically there was no interstitial fluid phase (Weinhart et al. 2013; Kamrin and Henann 2015). Here we compare the rheology determined from "instantaneous" CG analysis that involved the averaging of two timesteps (100 ms apart) on an unconfined bed (no top plate) versus time-averaging of 1000 time steps from shear cell simulations (data recorded during 100s). In the instantaneous case, we rotate the gravity vector slowly, whereas the time-averaged data involved 100 individual simulations of a sheared bed confined by two rough plates, wherein a force and velocity are imposed on the upper rough plate (Fig.1a). The wide range of inertial number spanning $1x10^{-6}$ to $2x10^{0}$ is investigated by changing either pressure or the shear rate in the shear cell simulations. In Figure 4a, we plot the Φ as a function of the log of the inertial number $log_{10}(I)$. Because there are very few fluctuations in the data, the $\Phi(I)$ law is directly recovered and takes the form:

$$\Phi(I) = \frac{\Phi_{max}}{1+aI} \quad \text{(Eq.18)}$$

with Φ_{max} being the maximum concentration and a being a constant found by fitting. The fit gives Φ_{max} = 0.583 and a=1.0.

Plotting the time-averaged CG data reveals that the time-averaged data fall within the field of instantaneous data (Fig.4b) and for inertial numbers below 10^{-5}, the friction coefficient is fairly constant. We fitted the classical $\mu(I)$-rheology (Eq.2) (Jop et al. 2006) to the instantaneous data, with μ_1 = 0.355, which is the static friction coefficient, $\mu_2 = 1.04$ and $I_0 = 0.289$ (Fig.4c). The good fit to the data however is restricted to I<0.6, as illustrated for the complete dataset of time-averaged data (Fig.4d). In fact, the $\mu(I)$-rheology predicts a plateau for the friction coefficient, whereas the data diverge from that law. The best fit to the time-averaged data using the Eq.2 gives μ_1 = 0.355, which is the static friction coefficient, $\mu_2 = 1.43$ and $I_0 = 0.81$ (Fig.7e). While it better matches the data for I>0.6, the fit in the intermediate regime at I >10^{-3} to 0.3 is fairly poor.

In order to describe the rapid increase of the friction coefficient with I at large inertial numbers, we plotted the following $\mu(I)$ law based upon the work of Holyoake and McElwaine (2012):

$$\mu(I) = \frac{\mu_s I_0 + \mu_d I + \mu_\infty I^2}{I_0 + I} \quad \text{(Eq.19)}$$

which involves the same parameters as in the classical *μ(I),* with μ_s is the static friction coefficient = μ_1, μ_d=μ_2 and I_0. There are also other constants that can be found by fitting the data such as μ_∞. By fitting Eq.19 to the data we found μ_1 = 0.355, μ_2 = 1.0, $I_0 = 0.3$ and $\mu_\infty = 0.18$ (Fig.7f). This provides a good agreement with the data for the whole range of inertial number investigated and suggests that a single simulation can be used to recover the *μ(I)* instead of using laboriously tens of individual simulations. This is very handy, in particular to investigate the role of DEM-CFD parameters or even to look at the effect of pore pressure on the granular rheology. Interested readers can visualize how the particle softness and particle restitution coefficient affect the bulk *μ(I) and* $\Phi(I)$ scaling (Fig. S4), which are commensurate with earlier findings of Chialvo et al. (2012). In addition, the presence of the interstitial fluid (air), which was included for completeness, has no measurable influence on the results and could have been excluded from simulations where no-excess pore pressure was investigated.

In order to check whether slight polydispersity could affect the flow rheology, we reproduce the polydispersity of d±0.2d used in the rheology experiments. The mean particle diameter was calculated at each timestep to account for size segregation in the CG analysis. The solid density follows the same trends as the monodisperse case (Fig.4g). Additionally, the friction coefficient also follows the same trend as the monodisperse counterparts for the intermediate and inertial regimes. However, there is evidence of the thermal creep regime in the data for $I<4\text{x}10^{-5}$, as suggested by the friction coefficient that becomes lower than the tangent of the angle of repose (=0.355). The fit thus requires the addition of the description of the decline of the friction coefficient with *I* for low inertial number, which has conveniently been provided by Barker et al. 2017. By adding a function describing the lowering of the friction coefficient below the static friction coefficient, one can describe the quasistatic, intermediate and inertial regimes with the following function:

$$\mu(I) = \begin{pmatrix} \sqrt{\frac{\alpha}{ln\left(\frac{A_1}{I}\right)}} & I \le I_1^N \\ Eq.\,21 & I > I_1^N \end{pmatrix} \quad \text{(Eq.20)}$$

$$A_1 = I_1^N \exp\left(\frac{\alpha\left(I_0 + I_1^N\right)^2}{(\mu_{static} I_0 + \mu_d I_1^N + \mu_\infty (I_1^N)^2)^2}\right) \quad \text{(Eq.21)}$$

where A_1, I_0, I_1^N, μ_∞, μ_d and α are constants. When used in continuum models, Eqs.20 and 21 ensure well-posedness for I = 0 to ~10 (Barker et al 2017).

Because the friction coefficient only differs from monodisperse at very low inertial numbers <~10^{-5} and because the role of polydispersity is beyond the scope of the present work, the following sections solely focus on monodisperse suspensions.

3.2.2 Non-fluidized versus fluidized bed rheology

In this section we qualitatively compare the rheology of sheared fluidized beds with that of the non-fluidized sheared beds. A good overlap for the *μ(I)* exists between the sheared fluidized and the non-fluidized beds for the intermediate and inertial regime. This is shown by adding the *μ(I)* fit from the time-averaged rheology simulations (from Fig.5a and b), which shows that it describes well the increase of μ at high inertial numbers.

4 Discussion

4.1 Friction coefficient in beds with excess pore pressure

Granular flow rheology is independent of the absolute pore pressure of the fluid phase in which it is immersed. However, pore fluid flow driven by pore pressure gradients and specifically excess pore pressure can modify the effective stresses in granular flows. This is particularly common in beds with a vertical gas flux, where the drag force opposes gravity and is known as fluidization. Fluidization (excess pore pressure) lowers the initial measured friction coefficient *μ(I)* in fluidized beds confined in a volume (bed dilates but does not flow in directions normal to gravity). This behavior is the result of drag-induced dilation, where friction is partially mobilized.

By contrast, in granular beds with excess pore pressure, which are allowed to flow (i.e. placed on an incline, or not physically constrained) depict a *μ(I)* systematically greater than the static friction coefficient due to particle collisions.

However, dam-break experiments on initially to partially fluidized beds show that the angle of repose is much lower than the angle of repose of the material in a non-fluidized state (Roche et al. 2005). Obtaining information regarding the friction properties of fluidized beds from such experiments is not possible since the flows are highly unsteady. Below, we reconcile our experimental observations of similar *μ(I)* between the fluidized and non-fluidized bed, the low

angle of repose of fluidized bed from damn-break experiments and the *μ(I)-rheology* measured in DEM-CFD simulations.

Most interesting is the effective friction of the bed and whether it equals the macroscopic friction, in particular for a sheared fluidized bed. We showed that the *μ(I)-rheology* of non-fluidized bed is similar to that of the fluidized counterpart. Such behavior entails that when fluidized, the solid pressure is significantly lower than lithostatic, thus raising the inertial number. Therefore, a question arising is whether sheared fluidized beds can reach steady state? On a 24° slope, we simulate a fluidized bed with a chosen superficial velocity of 1.5 m/s. For 7 seconds the flow was in a transient state before the solid concentration (Fig.6a), solid pressure (Fig.6b), shear rate (Fig.6c), inertial number (Fig.6d) and friction coefficient (Fig.6e) become constant. Once steady, we notice that the macroscopic friction coefficient of ~0.55 largely exceeds the tan(slope)=0.445 (Fig.6e), which by itself should prevent steady state to occur and suggest that the flow should progressively slow down.

We define the non-dimensional solid P_s^* (Fig.6a) and pore pressure P_g^* (Fig.6b) where:

$$P_g^* = \frac{P_g}{P_{hydrostatic}} = \frac{P_g}{\rho g h} \quad \text{and} \quad P_s^* = \frac{P_s}{P_{hydrostatic}} = \frac{P_s}{\rho g h} \quad \text{(Eq.22)}$$

The effective friction coefficients as either the ratio of the macroscopic friction and non-dimensional solid pressure or non-dimensional pore fluid pressure (Fig.6h).

$$\mu_{eff}(I, P_g^*) = \mu(I)\,(1 - \alpha P_g^*) \quad \text{and} \quad \mu_{eff}(I, P_s^*) = \mu(I)\,P_s^* \quad \text{(Eq.23)}$$

α is a coefficient that needs to be fitted and corresponds to the slope of the linear approximation of Ps*=f(Pg*), and takes a value of ~0.85±0.05 in calculations of the effective friction coefficient (Fig.6f and Fig.6g). The effective friction coefficients tend to tan(slope), thus explaining how steady state can be attained. This means that the effective friction coefficient needs to account for the degree of bed support either through the reduction of solid pressure or increase of pore fluid pressure to describe accurately a granular flow with pore pressure.

While the partially fluidized bed follows the $\mu(I)$*-rheology* (Fig.5), it behaves as a bed of equal mass on a steeper slope. Figure 6 shows that the dry bed on a 29° slope display the same i) inertial number, ii) $\mu(I)$, iii) solid concentration, but because the solid pressure of the fluidized bed is slightly lower, the shear rate is also lower than in the 29°-dry case. The value of 29° is found by simply taking the arc tangent of time-averaged $\mu(I)$ of the 24° fluidized case.

Following this finding, we investigate the steady state of fluidized beds under a range of pressures and slopes covering 15 to 30 degrees. When the bed reaches steady states, the effective friction

coefficient must be equal to the tan(slope). This is verified when calculating the effective friction coefficient using either the $\mu_{eff}(I, {P_g}^*)$ or $\mu_{eff}(I, {P_s}^*)$, as shown in Figure 6g.

The results have many implications for geological flows that can develop pore fluid pressure such as debris flows (Iverson 1997; Iverson et al. 2010) and pyroclastic density currents (also known as pyroclastic flows) (Roche et al. 2016; Gueugneau et al. 2017) as long as dilatancy is a function of the inertial number and pore pressure (fluid drag). Concentrated pyroclastic currents often form by collapse of a more dilute mixture (Branney and Kokelaar 2002) that enables pore pressure to form (Breard et al. 2017). In this case, the flows would behave with the effective friction defined in Eq.23. In the fields of debris flows, the role of bed support has been included in constitutive equations into the correction of the normal stress, defined in the basal shear stress as follows:

$$\tau_{base} = cos(\theta)\left(\sigma - P_g\right)\mu_s \quad \text{(Eq.24)}$$

where P_g is the pore fluid pressure, σ is the normal stress=solid pressure, μ_s is the coulomb friction coefficient of the granular material and θ is the slope of the substrate. A similar approach was used by (Gueugneau et al. 2017) and applied to pyroclastic flows. Without basal slip, the basal friction coefficient is equivalent to the $\mu(I)$ (GDR-MiDi 2004). Instead, with slip there are differences between the basal and internal friction coefficient (Breard et al. 2020). In this work, we do not study the basal friction coefficient and slip. Nevertheless, an equation similar to Eq.24 can be used to describe the internal shear stress at a given height in the flow. DEM-CFD simulations demonstrate that the friction itself is a non-linear function of the competing effect of the inertial number and most importantly, of the pore pressure. Thus, we write the constitutive equation for the internal shear stress as:

$$\tau = \mu(I)P_s = \mu(I)(\sigma - \alpha P_g) \quad \text{(Eq.25)}$$

σ is the lithostatic pressure defined as ρgh, P_g is the pore fluid pressure, α is the slope correlating the solid to pore fluid pressure (=0.86). Note that a more complex function (non-linear scaling of the solid pressure from pore pressure measurements) could be used, but the relatively good match of the linear fit (R-sq = 0.96) is appealing.

While the inertial number increases the friction coefficient, the effect of the pore pressure is thus weakening the effective friction coefficient by the means of reducing the effective normal stress $\sigma - \alpha P_g$. The inclusion of the $\mu(I)$ term is essential because friction in simulated beds increases from 0.35 to 0.9 while the normalized solid pressure is lowered from 1 to 0.2.

581 This interpretation is analogous to Terzaghi's principle (Terzaghi 1936), which introduced the
582 concept of effective stress, which is the total stress exerted by the solid "skeleton" minus the pore-
583 fluid pressure in water-saturated soils.
584 $\sigma_{ij}' = \sigma_{ij} - P_g \delta_{ij}$ (Eq.26)
585 δ_{ij} is the Kronecker's delta.
586 However, our definition differs from Terzaghi's through the need to use a coefficient α.
587
588 This work is topical to many applications, as illustrated by how pore pressure and the subsequent
589 effective friction can influence failure of a granular flow on an incline. In the next section, we
590 discuss the destabilization of fluidized beds on incline slopes and explore the meaning of the
591 coefficient α.
592
593
594 **4.2 Failure of granular flows by progressive fluidization**
595 A bed is placed on a 15° slope (3.5° lower than the angle of repose) and the superficial gas velocity
596 is increased after 2 seconds following the linear law 0.1+0.04*(time-2). The results and following
597 conclusions are independent of the rate at which the gas velocity was changed (Fig. S2).
598 Without any superficial velocity the bed experiences creeping, since it rests on a slope lower than
599 the angle of repose. For superficial velocity <1.2 m/s, the bed remains in the quasistatic regime
600 with a shear rate of 10^{-4} to 10^{-2} Hz and a granular temperature that mimics the shear rate data
601 (Fig.7a). The scaled solid pressure P_g^* and pore pressure 1-P_g^* data mirror one another (Fig.7b)
602 while the fractional solid fraction (Φ/Φ_{start}) declined by 1% (Fig.7c). Meanwhile, the friction
603 coefficient μ(I) increases from values of 0.36 to 0.46, whereas the effective frictions μ(I,Ps*) and
604 μ(I,Pg*) decline and once reaching ~tan(15°), the bed fails.
605 The failure of the bed which follows the increase in pore pressure and subsequent decrease of the
606 effective shear stress is analogous to liquefaction, which operates in saturated soils (Iverson et al.
607 1997). Our results are commensurate with the concept of shear strength defined by the Tergazhi-
608 Coulomb criterion, which states that failure can only occur if the effective friction coefficient
609 is<tan(slope). Consequently, dilation of the bed is small enough (up to 1%) for the Tergazhi's
610 principle to be valid.
611 The failure is followed by a rapid change in all bed properties. The sudden dilation led to a decrease
612 of P_g^* and subsequent increase of P_s^*. The bed rapidly recovers and all trends mimic those seen

prior to failure. The ability of the bed to fail and accelerate on a slope much smaller than the measured μ(I) is captured by the definition of the effective friction coefficient which encapsulate the effective stress. Past the failure point, the bed is flowing and Tergazhi's principle is not the most appropriate description of the effective stress (and effective friction coefficient). Instead, the effective shear stress is better described by equation 26 where the proportion of pore pressure alleviating the shear stress is non-unity because shear developed. In other words, even when fully fluidized, the effective shear stress is non-zero because particle interactions generate a normal stress. This is exemplified when plotting the dimensionless solid pressure Ps* as a function of the the dimensionless pore pressure Pg* (Fig.8a).

The introduction of a coefficient in Eq.25 resembles the description of effective stress introduced by Biot (1962), where α, known as the "Biot effective-stress coefficient" noted α_b, is the proportion of fluid pressure which will induce the same strains as the total stress. In solid mechanics, $\alpha_b = 1 - \frac{K_m}{K_s}$. K_m is the Bulk modulus of the porous media (or volume compressibility of the matrix) and K_s is the bulk modulus of the solid (or volume compressibility of the minerals/grains comprising the matrix). Hence, for incompressible mixtures, α_b=1 and recovers Terzaghi's principle. However, our system is not a dense porous static media with deformable particles. Instead, particles in our simulations are "hard" spheres, where the high spring constant makes the particle overlap in the spring-dashpot model <1% of their diameter. Therefore, the compressibility of the solid grains is not the cause behind the value of the coefficient α.

The normal stress (solid pressure) is not vanishing in our simulations because the shear stress is made of both the contact and kinetic contributions (see Eqs.11, 14, 15), which means that as long as there are velocity fluctuations (even if they were no contacts between particles), the shear stress cannot be null. As shown in Fig.7a, the granular temperature is $\sim$0.25 m^2/s^2 at the end of the simulation, which is very large. For comparison, it is $\sim 10^{-9}$-10^{-10} m^2/s^2 in the quasistatic regime prior to failure (Fig. 8a). The observation of a non-zero shear stress when the bed is fully fluidized and sheared is commensurate with the predictions of Kinetic Theory (Jessop et al. 2017), which includes the contribution of the granular temperature to the bulk stress tensor. Typically, models that use Terzaghi's principle (usually used for liquid-solid mixtures such as debris flows) make two assumptions: the kinetic stress is null and the solid pressure is isotropic. Both assumptions can be tested in our gas-particle system. First, the contact contribution to the pressure (Ps^{c*}) only is plotted against the dimensionless pore pressure Pg*, and shows a linear fit with a slope of 0.95 (Fig.8b). Second, we plot the dimensionless y-component (vertical) of solid pressure from the

645 contact contribution (Ps^{c*}_{y}) against Pg*, giving a linear fit with a slope of ~1 (Fig.8c). Thus, we
646 interpret $\alpha = 0.86$ as the result of both the contribution of the kinetic stress tensor and anisotropy
647 of the solid pressure. This conclusion holds for the range of spring constant (100-10000 Pa.m),
648 particle-particle restitution (0.1-0.9) and friction coefficients (0.1-0.5) explored (Fig.8a-8c), with
649 specific values of α span the range of 0.84-0.9 (Fig.8a). Observing similar deviation from Terzaghi's
650 principle in experimental flows, particularly with high polydispersity, will be highly valuable and
651 yet challenging to obtain as it will require simultaneous measurements of the (basal) solid
652 pressure in 3D and pore fluid pressure.
653
654 **4.3 Depth-averaged models of granular flows immersed in a fluid.**
655 The role of pore pressure has long been recognized as the essential property controlling the
656 rheology of debris flows modifying the flow rheology from Coulomb solid to a viscous fluid
657 (Iverson 1997; Iverson et al. 1997; Iverson et al. 2010). Additionally, the formation of pore
658 pressure during ground shaking can produce liquefaction of soils which facilitates the formation
659 of landslides. Similarly, gas-particle flows can experience a similar effect, where fluidization is a
660 result of pore pressure formation and changes the solid concentration. This process is envisaged
661 in pyroclastic flows, where the presence of high pore pressure has been hypothesized for decades
662 as the origin behind the extreme mobility of these concentrated currents (Brown 1962; Sparks
663 1976; Wilson 1980; Wilson 1984; Freundt 1998; Druitt et al. 2004; Girolami et al. 2007; Montserrat
664 et al. 2012; Roche 2012; Breard et al. 2017; Breard et al. 2019).
665 In the past decades, natural granular flows have been simulated using a depth-averaged method
666 that uses the shallow water equations to solve the mass and momentum equations of a single phase
667 (solid) moving across 3D topographies (Charbonnier and Gertisser 2009; Capra et al. 2011;
668 Kelfoun 2011; Charbonnier et al. 2013; Lucas et al. 2014; Kelfoun 2017; Ogburn and Calder 2017;
669 de' Michieli Vitturi et al. 2019; Gueugneau et al. 2020). The depth-averaged method is particularly
670 useful to understand the behavior or past and future events for quantitative hazard assessment.
671 The strength of a single-phase depth-average model is in their speed and ability to capture the
672 forcing of topography on the flow behavior. However, such approach does not describe the gas-
673 particle coupling (i.e. pore-pressure feedback) and its effect on the effective stresses of the
674 granular mixtures. Recently, an emergent technique relies on two-phase models that capture the
675 interactions between the fluid and solid phases within a saturated mixture, which is particularly
676 relevant to predict the emplacement of debris flows or submarine avalanches (Iverson and George

2014; Bouchut et al. 2016). This method is able to capture the inherent compressibility of granular media (i.e. compaction or dilation) using a dilation angle ψ, which affects the friction and pore-fluid pressure and known as pore-pressure feedback. In these models the shear stress is written as:

$$\tau = [\mu(I) + \tan\psi]\left[\sigma - P_g\right] \quad \text{(Eq.27)}$$

σ is the normal stress, P_g is the excess pore pressure, ψ is the dilatancy angle. In two-fluid models work, the effective friction coefficient is equal to $\mu(I) + \tan\psi$. The dilatancy, dilation rate $\nabla \cdot v_s$ and shear rate $\dot{\gamma}$ are related as follows:

$$\nabla \cdot v_s = \dot{\gamma} \tan\psi \quad \text{(Eq.28)}$$

Where the divergence of the solid velocity $\nabla \cdot v_s$ can estimated as from the temporal changes in solid concentration Φ:

$$\nabla \cdot v_s = -\frac{1}{\Phi}\frac{d\Phi}{dt} \quad \text{(Eq.29)}$$

This implies that in a steady state $\tan\psi = 0$. In the simulations we presented in this paper, $\tan\psi < 0.03\ \mu(I)$. Therefore, the contribution of $\tan\psi$ to the friction coefficient was negligible.

Adapting two-phase flow models for gas-particles flows and including a compressible gas phase could provide a significant leap towards the accurate prediction of the behavior of gas-particle granular flows. Such model would need to capture (a) the dilation and compaction of granular flows and how changes in solid concentration modulates pore-fluid pressure, (b) the non-vanishing of the granular shear stress in highly inertial sheared fluidized beds when the pore pressure equals the "static" solid pressure, and finally (c) role of anisotropy of the flow properties. Continuum granular flow models like that of Bouchut et al. (2016) assumes that granular temperature is negligible in the context of grains immersed in water. We show that in our simulations. Such assumption would not be valid in our gas-particle simulations, particularly for $I > 0.1$, for the contribution to the solid pressure was between 1–20%.

Therefore, accurate description of gas-particles granular flows in a continuum framework requires a description of velocity fluctuations as a function of other bed properties such as the inertial number, normal and shear stresses, which may be further complexified by the existence of stress and granular temperature anisotropies (e.g. See Fig.8 in Breard et al. 2020).

4.4 Suspension and granular rheology of fluidized and non-fluidized beds

In the past, fluidized granular systems were systematically associated with suspensions, which has led to an incorrect prediction of their viscosity (Gibilaro et al. 2007). Such assumptions can impede

our ability to predict the behavior of fluidized geophysical systems, which encompass mass flows and even magmas. Here, we show the viscosity of a granular bed with and without the presence of pore pressure can be expressed by accounting for particle collisions. Note that the following section only applies to granular flows with a Stokes number >>1.

When a suspension is sheared, we can express the shear and normal stresses (=solid pressure) as a function of the fluid viscosity, shear rate and solid concentration:

$$\tau = \eta_s(\Phi)\,\eta_f\,\dot{\gamma} \quad \text{and} \quad P_s = \eta_n(\Phi)\eta_f\,\dot{\gamma} \quad \text{(Eq.30)}$$

where η_s and η_n are the dimensionless shear and normal viscosities respectively (Stickel and Powell 2005). As shown in figure 5b the sheared non-fluidized and fluidized bed display a dilatancy law that is a function of the inertial number. Thus, we can write dimensionless effective shear and normal viscosities as (Andreotti et al. 2013):

$$\eta_s(\Phi) = \frac{\mu\,(I(\Phi))}{I(\Phi)^2} \text{ and } \eta_n(\Phi) = \frac{1}{I(\Phi)^2} \quad \text{(Eq.31)}$$

We can write the friction coefficient of the suspension as a function of the hydrodynamic and contact contributions, combined linearly. The constitutive relation is defined as:

$$\mu\left(I(\Phi)\right) = \mu^c(\Phi) + \mu^h(\Phi) = \mu_1 + \frac{\mu_2-\mu_1}{1+\frac{I_0}{I}} + I^2 + \frac{5}{2}\frac{\Phi_{max}}{a}\,I \quad \text{(Eq.32)}$$

The terms in red represent the contact contributions which is similar to that of granular media whereas the terms in blue represent the hydrodynamic contribution that recovers the Einstein viscosity at low concentration (Einstein 1905). This model is in agreement with the unified rheology of viscous suspensions defined by (Boyer et al. 2011).

Here, the dilatancy law observed has an asymptotic form and allows us to write the inertial number as a function of the concentration:

$$\Phi(I) = \frac{\Phi_{max}}{1+aI} \quad \text{or } I = \frac{\Phi_{max}-\Phi}{a\Phi} \quad \text{(Eq.33)}$$

Hence, the non-dimensional shear viscosity is given by replacing Eq.(31) and Eq.(33) in Eq.(31):

$$\eta_s = \frac{\mu^c}{I^2} + 1 + \frac{5}{2}\,\Phi\,(1-\frac{\Phi}{\Phi_m})^{-1} \quad \text{(Eq.34a)}$$

The same equation can be written as a function of the concentration only using a fitted parameter "a":

738 $\eta_s = \mu^c(\Phi)a^2(\frac{\Phi}{\Phi_m-\Phi})^2 + 1 + \frac{5}{2}\Phi\,(1-\frac{\Phi}{\Phi_m})^{-1}$ (Eq.34b)

739 with $\mu^c(\Phi) = \mu_1 + \frac{\mu_2-\mu_1}{1+\frac{I_o}{\left[\frac{\Phi m-\Phi}{a\Phi}\right]}}$ (Eq.35)

740 The term $1+\frac{5}{2}\Phi\,(1-\frac{\Phi}{\Phi_m})^{-1}$ is the hydrodynamic contribution, which recovers that defined by

741 Einstein [1905] at low Φ (<0.05):

742 $\eta_{s\_Einstein}$=1+5Φ/2 (Eq.36)

743 The CG analysis provides measurements of the friction coefficient μ^c, inertial number I and solid

744 concentration Φ. Thus, we can calculate the shear viscosity using Eq.34a (Fig.9a). The shear

745 viscosity data derived from our simulations is plotted against the Krieger and Dougherty (1959)

746 empirical expression of the non-dimensional shear viscosity of non-Newtonian suspensions:

747 $\eta_r = (1-\frac{\Phi}{\Phi_m})^{-2.5\Phi_m}$ (Eq.37)

748 Our data collapses onto the empirical curve where Φ_m =0.583 for the non-fluidized (Fig.9a) and

749 fluidized beds (Fig.9b). Our results show that the suspension rheology describes efficiently the

750 granular contribution to the viscosity for fluidized and non-fluidized beds.

751 These results are, to our knowledge, the first quantification of the shear viscosity of fluidized and

752 non-fluidized beds with gravitational forces compared to simulations or experiments where the

753 fluid and particles have the same density (Boyer et al. 2011).

754 Using the unification of suspension and granular rheology, we simulate fluidized beds prior to

755 bubbling and calculate the mixture viscosity. Multiple experiments with 100 microns particles

756 (Grace 1970; King et al. 1981; Rees et al. 2005) have shown that gas fluidized bed viscosities could

757 not be explained by classical laws using a pseudo-fluid assumption such as:

758 $\eta_{app}(\Phi) = (1+2.8_s\Phi)\,\eta_f$ (Eq.38) (Gibilaro et al. 2007)

759 The above equation predicted viscosities that were lower than measurements by orders of

760 magnitude. Therefore, Gibilaro et al. (2007) attributed the large discrepancy to the particle-

761 particle interactions, lacking in a pseudo fluid assumption. To demonstrate that granular rheology

762 controls viscosity of fluidized beds, we simulated a fluidized bed of 100 microns beads of density

763 equal to that of glass beads (2500 kg.m^{-3}) from the onset of minimum fluidization to the onset of

764 bubbling, and estimated the mixture viscosity:

765 $\eta_{app} = \eta_s(\Phi)\,\eta_f$ (Eq.39).

766 The viscosity of the simulated fluidized bed falls within the 0.08–1 Pa.s range (Fig.9c), which

767 corresponds to the range of measurements from experimental measurements. These results

768 confirm that an accurate description of the shear viscosity that includes the granular rheology can
769 predict the viscosity of fluidized beds.
770
771
772 **4.5 Application to geophysical flows and implication for substrate erosion**
773 Field evidence indicates re-entrainment of freshly deposited pumice and ash deposits often occurs
774 (Druitt et al. 2002) and can significantly increase the volume of the current. However, the
775 mechanisms behind the erosion of fine-grained substrate remains an open question (Roche et al.
776 2013). To illustrate how the granular rheology and pore pressure influences the erosion process,
777 we simulated the basal portion of non-fluidized (Fig.10a) and fluidized beds (Fig.10b) on a
778 horizontal plane. The simulations illustrate best the high complexity of granular media with and
779 without pore pressure. For instance, the non-fluidized (=pressure-balanced) case displayed effects
780 of non-locality at t=0s with a friction coefficient in the erodible bed and lower part of the sheared
781 bed case (Fig.10a) lower than the static coefficient (=0.355). The gradient in shear rate induced
782 small vibrations that propagated from the upper part of the flow onto the bed underneath which
783 is in the quasistatic regime, yielding flowage at $\mu_{eff} < \mu_s$. This is known as a non-local granular
784 fluidity effect (Kamrin and Koval 2012) and was recently attributed to the diffusion of granular
785 temperature (Kim and Kamrin 2020). A second after the onset of erosion, the friction coefficient
786 increases $>\mu_s$, and few particles from the substrate were incorporated within the basal portion of
787 the flow. Furthermore, in the fluidized case, we simulated the lower portion (lower 0.05m) of a
788 thick fluidized flow that at t=0 did not diffuse the pore pressure into the lower bed yet. At that
789 stage, the μ_{eff} is about 0.1–0.15 because of the effect of pore pressure, while non-local fluidity
790 affects the erodible bed. Within a second, erosion was well underway with a shear rate two orders
791 of magnitude higher in the former substrate, newly part of the flow. The pore pressure lowered
792 μ_{eff} to 0.03–0.06, which enable rapid mobilization of the substrate.
793 We hypothesize that when dense pyroclastic density currents (pyroclastic flows) propagate over
794 a substrate, the flow compacts the substrate because of the rapid increase of the confining solid
795 pressure (Fig.S5). Compaction forces upward diffusion of the excess pore pressure from the
796 substrate into the flow, thus lowering the effective friction coefficient of the substrate. A similar
797 mechanism has been proposed in snow avalanches and debris flows (Iverson et al. 2010; Gauer
798 and Issler 2017). Through this process, the shear stress applied by the flow upon the substrate can
799 overcome its yield strength (which was weakened first by non-locality) and the substrate will be

800 entrained into the flow. As demonstrated, this erosion process would occur even on shallow slopes,
801 well below the angle of repose of volcanic deposits (~30–40 degrees).
802 Lowering of the friction coefficient of the substrate is not restricted to granular flows with pore
803 pressure. In fact, the role of non-local effects can be at play in non-fluidized granular flows devoid
804 of excess pore pressure, by simply applying shear gradients upon the substrate, we show that the
805 friction coefficient of the latter is weakened, which in turns promote entrainment even on slopes
806 lower than the static angle of repose.
807 To demonstrate that velocity fluctuations are the source of the non-local behavior and weakening
808 of the substrate, we defined the dimensionless granular temperature as in Kinetic Theory:
809 $\Theta = \rho_s T_g / P_s$ (Eq.40) (Lun et al. 1984).
810 Following the work of Kim and Kamrin (2020), we illustrate non-local behavior in a set of 23
811 simulations where a sheared bed moves atop an erodible substrate with an inertial numbers
812 spanning value of 10^{-4} to 10^{0} (Fig.10a-c). Velocity fluctuations propagate spatially in granular flows
813 through contact forces that can take the form of force chains. Our simulations mimic the arrival of
814 flows spanning quasistatic to inertial regimes and the onset of erosion of the substrate underneath.
815 The development of non-locality is quantified using the scaling of the friction coefficient $\mu(I, \Theta)$,
816 which is a function of both the inertial number and the dimensionless granular temperature. The
817 local $\mu(I) - rheology$ model predicts vanishing shear rate for $\mu < \mu_{static}$. However, we observe a
818 creeping region with non-zero shear in such region where the friction coefficient in the substrate
819 deviates from the $\mu(I)$ (Fig.10d). The connection between the granular temperature and $\mu(I)$
820 becomes clear with the formulation:
821 $$\mu(I, \Theta) = \left(\frac{\Theta_{loc}(I)}{\Theta}\right)^{1/6} \mu_{loc}(I) \quad \text{(Eq.41)}$$
822 Where both $\mu_{loc}(I)$ and $\Theta_{loc}(I)$ are determined in simple shear flows (i.e. shear cell without non-
823 erodible rough substrate). The collapse of our data and the description presented in Eq.41
824 illustrates that as granular temperature increases, the friction coefficient of the granular mixture
825 will be lowered (Fig.10e).
826 As demonstrated by Kim and Kamrin (2020) (See their Fig.2), the friction-weakening of a granular
827 media by diffusion of granular temperature is not restricted to region where the inertial number
828 is $<10^{-3}$, but can occur up to $I \sim 10^{-1}$ (on steep slopes). Such settings are expected to occur in nature,
829 with pyroclastic density currents propagating on steep volcanic slopes and snow-avalanches on
830 snow-clad mountainous flanks.

We have proposed that gas-particle beds with pore pressure (or fluidized beds) rheology combines suspension and granular rheology with the addition of a friction-weakening mechanism ascribable to dilation due to pore pressure diffusion. These results are paramount for understanding the behavior of static and sheared gas-particle granular beds that prevail in many natural environments. Including the contribution of $\mu(I)$ and excess pore pressure in a description of the effective friction coefficient into numerical models such as depth-averaged models (Kelfoun 2011; Gueugneau et al. 2017) could advance the reliability of the models generally used to assess mass flow hazards by providing robust rheological laws.

Presently, the rheology of most natural geophysical mixtures, in particular of volcanic ash, remain completely unknown, in comparison with simplified sand or glass bead mixtures (Forterre and Pouliquen 2008). Studies of natural mixtures through experiments will be essential not only to further our understanding of the steady-state rheology, but most importantly, of the transient state as well. In addition, the polydispersity of natural mixtures will influence the flow rheology through size and density segregation, adding to the transience of the mixture rheology. Finally, future analog experiments should focus on measuring granular temperature (even in 2D) to help understand non-locality in granular media and bridge the gap between the discrete and continuum descriptions of granular flows.

5. Conclusion

In this study of gas-fluidized and non-fluidized granular flows we highlighted the main contribution of the pore pressure in the flow rheology. The combination of 3D DEM-CDF and coarse graining (CG) analysis enabled us to study the rheology of sheared granular flows across the whole spectrum of non-fluidized to bubbling fluidized beds. We showed that the *μ(I)-rheology* (friction) and $\Phi(I)$ (dilatancy) laws across the quasistatic, intermediate and inertial regimes could be recovered by simply running a CG analysis on 2 timesteps (0.1s apart) in a single simulation and provided similar results compared to time-averaged steady state simulations. The data is described well by the *μ(I)* description of Holyoake and McElwaine (2012), which does not predict an asymptotic behavior of the friction at large inertial numbers (>0.2).

Furthermore, in granular flows where pore pressure diffusion occurs (=fluidized bed), an effective friction coefficient governs their behavior and scales with the product of the $\mu(I)$ and relative pore pressure or solid pressure. Both the $\mu(I)$ and excess pore pressure have opposing effects on the

effective friction coefficient. As the pore pressure increase in a granular flow, drag-induced dilation generates a solid pressure decrease. By being allowed to move more freely, particle collisions induce an increase of the friction coefficient. The addition of drag-induced dilation to granular dynamic dilatancy makes a fluidized bed on a slope behave as if that slope was steeper by a factor scaled with the normal stress reduction. This process is captured by the definition of an effective friction coefficient. Importantly, our results suggest that both the effects of pore pressure and $\mu(I)$ should be accounted in the constitutive equations of gas-particle flows where pore pressure can form, as it is commonly done in the debris-flow community. In addition, on an incline, fluidized beds dilate because of particle collision. As a result, the kinetic stress tensor (which is a function of granular temperature) has a large contribution (up to 20%) to the total shear stress and solid pressure. Consequently, the shear stress in sheared fluidized beds (i.e. moving on inclines) does not vanish even if the excess pore pressure balances the lithostatic pressure completely. Therefore, Terzaghi's principle of effective stress for sheared fluidized beds (i.e. normal stress is null when fully fluidized) underestimates the shear stress. Instead, an explicit calculation of the granular temperature is needed to better capture the rheology of granular flows with excess pore pressure. In other words, the use of two-phase depth-averaged models to describe natural gas-particle flows will need to account for both the compressibility of the fluid phase and the contribution of the velocity fluctuations (in the inertial regime at I>0.1) to the stress tensor to accurately predict the inundation area of such currents.

Simulations illuminate how the viscosity of non-fluidized and fluidized beds could be expressed as a function of the contact and hydrodynamic contributions, thus unifying the suspension and granular rheology. Using a similar description, we showed that the viscosity of fluidized bed could be predicted and match experiments.

Finally, we illustrated the role of pore pressure beyond its modification of the sheared bed rheology, and in particular, its effectiveness for entrainment of an erodible substrate. We show that nonlocal effects occur when a granular flow propagates over an erodible substrate and that such behavior is the result of the diffusion of velocity fluctuations. Beyond the fundamental applications of this work, these results further our understanding of natural granular systems. They are particularly topical for geophysical flows where excess pore pressure can drastically affect flow mechanics (i.e. pyroclastic currents and snow avalanches).

Acknowledgements

Financial support was provided by the National Science Foundation (EAR 1852569 and EAR 1650382) and MCIU/AEI/FEDER, UE (Grant No. PGC2018 336 097842-B-I00). The research of LF was supported by the Royal Society of New Zealand (MAU1712). The research of MT was supported by La Caixa. The data supporting the conclusions are shown in the figures and tables presented. Interested readers will find additional data in the supporting information. On request the authors can also provide more specific results obtained from the experimental and numerical studies used to produce the figures.
ECPB thanks F. Bouchut and M. Yang for useful discussions.

Code availability.

The code used to produce the CFD is publicly available at https://mfix.netl.doe.gov.

Compliance with ethical standards Conflict of interest

The authors declare that they have no conflict of interest.

Table and figure captions:

Parameter [units]	Variables	Values
Domain size [m]	x, y, z	0.1x0.1x0.5
Grid size [m]	DX, DY, DZ	0.01
Fluid temperature [K]	T_g	293.15
Fluid dynamic viscosity [Pa s]	μ_f	1.8×10^{-5}
Particle density [kg.m^{-3}]	ρ_f	2500
Particle diameter [m]	d_p	0.005
Initial bed height [m]	H_0	0.1
Number of particles	N	9508
Particle stiffness (normal) [N.m^{-1}]	k_n	5×10^4
Particle normal restitution coefficient	e_n	0.5
Particle coefficient of friction	$\mu_{p\text{-}p}$	0.5
Particle-wall coefficient of friction	$\mu_{p\text{-}w}$	0.5

Table 1: Summary of the DEM-CFD simulation parameters used by default. Additionally, a set of simulations involved changing a single parameter, thus keeping all other quantities equal.

Figure #	DEM-CFD simulation type

2	1.1
3	1.2
4	2.1 and 2.2
5	1.2 and 2.1
6	1.2
7	1.2
8	1.2
9	1.2 and 2.1
10	3
11	3

Table 2: Types of DEM-CFD simulation from which the data is exported and presented in the different figures of the manuscript.

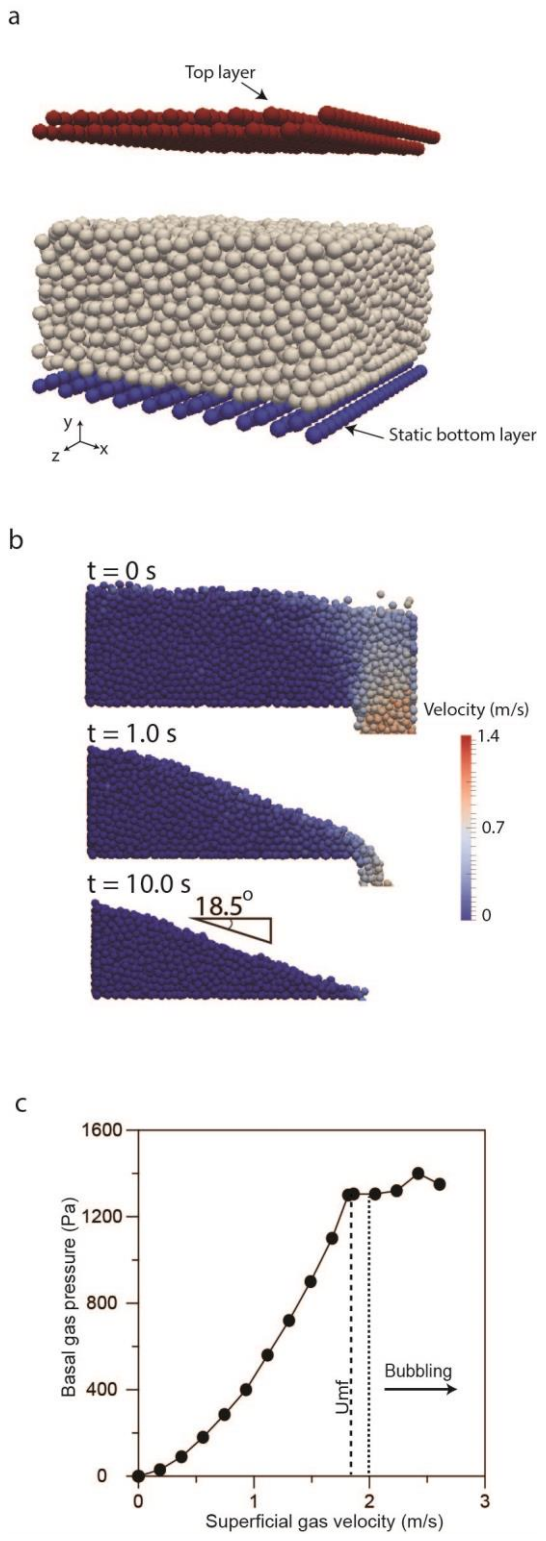

Fig.1a: DEM-CFD setup composed of a bed (white), that is constrained between the sheared top rough layer (red) and a bottom static rough layer (blue). **b**: DEM-CFD simulation of a dam-break collapse of the granular mixture of 5 mm beads in 3D. Periodic boundaries were used in the Z direction (normal to the plane shown), and the depth of the domain was equal to 0.05 m. DEM-CFD

parameters used are summarized in Table 1. **c:** Results of 16 steady state simulations are shown, by plotting the superficial gas (air) velocity versus the pore fluid pressure at the base of a 0.1 m thick bed of 5 mm beads (Table 1, for physical properties).

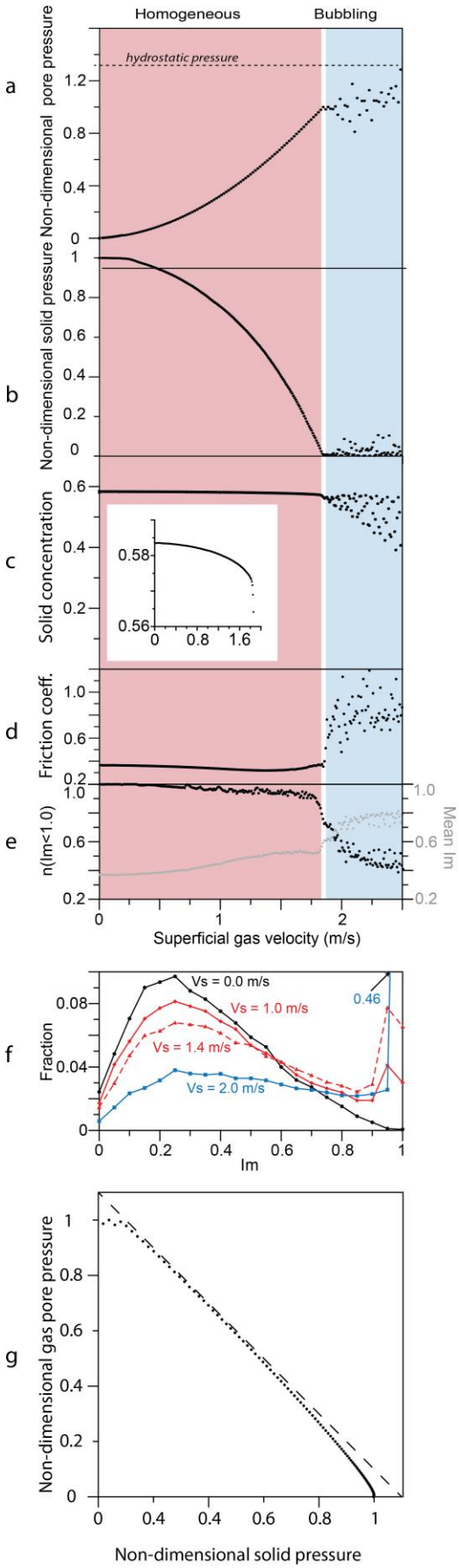
Homogeneous
Bubbling
hydrostatic pressure
a
Non-dimensional pore pressure
b
Non-dimensional solid pressure
c
Solid concentration
d
Friction coeff.
e
n(Im<1.0)
Mean Im
Superficial gas velocity (m/s)
f
Fraction
Vs = 0.0 m/s
Vs = 1.0 m/s
Vs = 1.4 m/s
Vs = 2.0 m/s
0.46
Im
g
Non-dimensional gas pore pressure
Non-dimensional solid pressure

Fig.2: Fluidization simulation of a confined bed on a horizontal plane. The CG analysis was undertaken in the lower 0.04m above the rough substrate. The solid pressure (**a**), solid concentration (**c**), friction coefficient (**d**), proportion of particle contacts n(*Im*<1.0) that not sliding and mean Friction Mobilization Factor (**e**) are plotted, while the excess pore pressure (**b**) data shown is at 0.005m above the rough plate. The insert in (c) shows the concentration (y-axis) as a function of the superficial gas velocity (x-axis) and illustrate the small but measurable dilation that occurs. For all particle contacts, we calculated the Friction Mobilization Index (*Im*), which is the ratio $Ft/(Fn \times \mu_{pp})$, where Ft and Fn are the magnitude of the tangential and normal contact force, respectively, and μ_{pp} is the particle-particle friction coefficient we used in the DEM code (=0.5). The distribution of Im for all contacts are shown at four different superficial velocities (V_s) in (**f**). A contact is mobilized (i.e. sliding occurs between two particles) when *Im*=1. Non-dimensional excess pore pressure is plotted against the non-dimensional solid pressure for the homogenous regime (**g**). The pore pressure and solid pressure are scaled to the lithostatic pressure measured when no air is injected in the mixture (non-fluidized).

The red background highlights the homogeneous regime, devoid of bubbles and prior to minimum fluidization at $V_s = V_{mf} \sim 1.85$ m/s. The blue background shows the bubbling regime, where bubbles propagate upward through the bed.

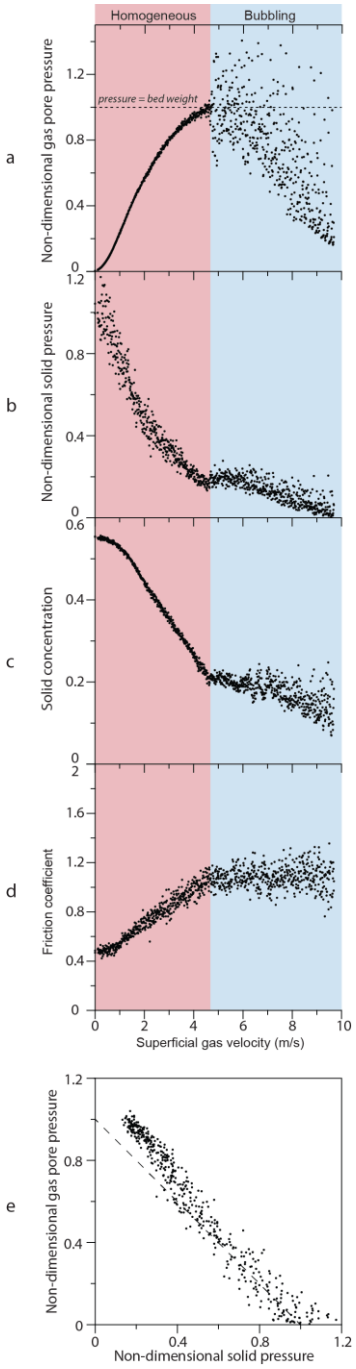

Fig.3: Fluidization simulation of a sheared bed on a 24° slope. The solid pressure (**a**), solid concentration (**c**) and friction coefficient (**d**) are plotted, while the pore pressure (**b**) data shown is at 0.005m above the rough plate. Non-dimensional pore pressure is plotted against the non-dimensional solid pressure for the homogenous fluidization regime. The dashed line shows a slope of 1. The pore pressure and solid pressure are scaled to the lithostatic pressure at the measurement location when no air is injected in the mixture (non-fluidized).

959 The red background highlights the homogeneous regime, devoid of bubbles and prior to minimum
960 fluidization at $V_s = V_{mf} = 4.46$ m/s. Bubbling is highlighted with the blue background whereas
961 homogenous fluidization is shown with the red background.
962

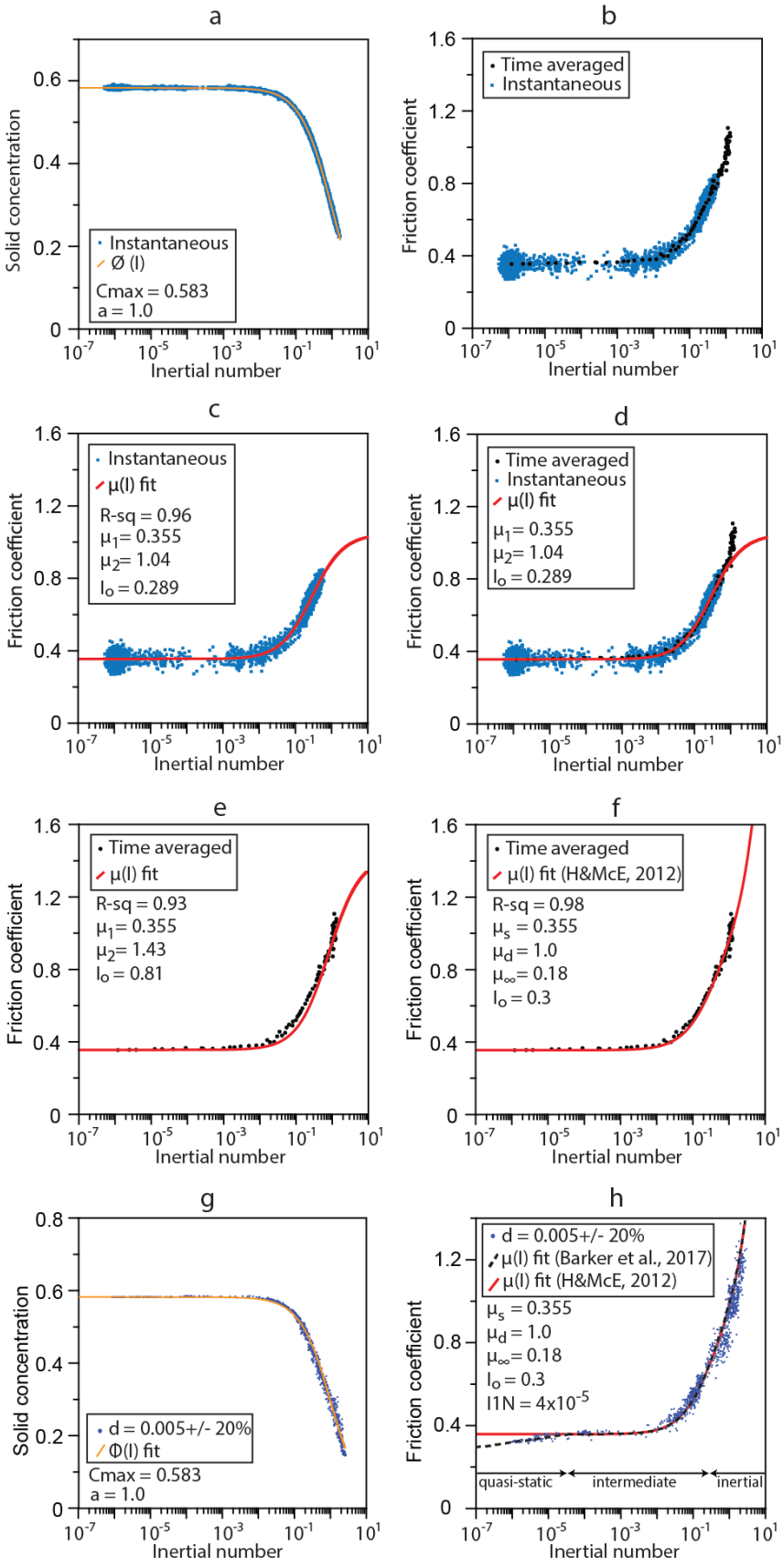
a
Solid concentration
Inertial number
Instantaneous
Ø (I)
Cmax = 0.583
a = 1.0
b
Friction coefficient
Inertial number
Time averaged
Instantaneous
c
Friction coefficient
Inertial number
Instantaneous
μ(I) fit
R-sq = 0.96
μ1= 0.355
μ2= 1.04
Io = 0.289
d
Friction coefficient
Inertial number
Time averaged
Instantaneous
μ(I) fit
μ1= 0.355
μ2= 1.04
Io = 0.289
e
Friction coefficient
Inertial number
Time averaged
μ(I) fit
R-sq = 0.93
μ1= 0.355
μ2= 1.43
Io = 0.81
f
Friction coefficient
Inertial number
Time averaged
μ(I) fit (H&McE, 2012)
R-sq = 0.98
μs = 0.355
μd = 1.0
μ∞= 0.18
Io = 0.3
g
Solid concentration
Inertial number
d = 0.005+/- 20%
Φ(I) fit
Cmax = 0.583
a = 1.0
h
Friction coefficient
Inertial number
d = 0.005+/- 20%
μ(I) fit (Barker et al., 2017)
μ(I) fit (H&McE, 2012)
μs = 0.355
μd = 1.0
μ∞= 0.18
Io = 0.3
I1N = 4x10-5
quasi-static
intermediate
inertial

Fig.4: Rheology of the non-fluidized bed. **a**: Solid concentration versus inertial number for the instantaneous CG analysis. **b**: Time-averaged (each black data point is an individual simulation) versus instantaneous friction data (blue dots) against inertial number calculated from the CG analysis. **c**: Instantaneous friction data with the $\mu(I)$ fit (red line) was added (Jop et al. 2006) with the fitting parameters shown in the legend. **d**: Instantaneous and time-averaged friction data with the $\mu(I)$ fit from figure (c). **e**: $\mu(I)$ fit (Jop et al. 2006) to the time-averaged data. **f**: $\mu(I)$ fit from Holyoake and McElwaine (2012) to the time-averaged data. **g**: Solid fraction versus inertial number for the slightly polydisperse bed of particle diameter 5±1 mm. The yellow line represents to fits to the data in figure a. **h**: Friction versus inertial number for the same mixture as in (g). The red line is the fit from (f), and the black dotted line is the description of Barker et al [2017] (Eqs.20 and 21).

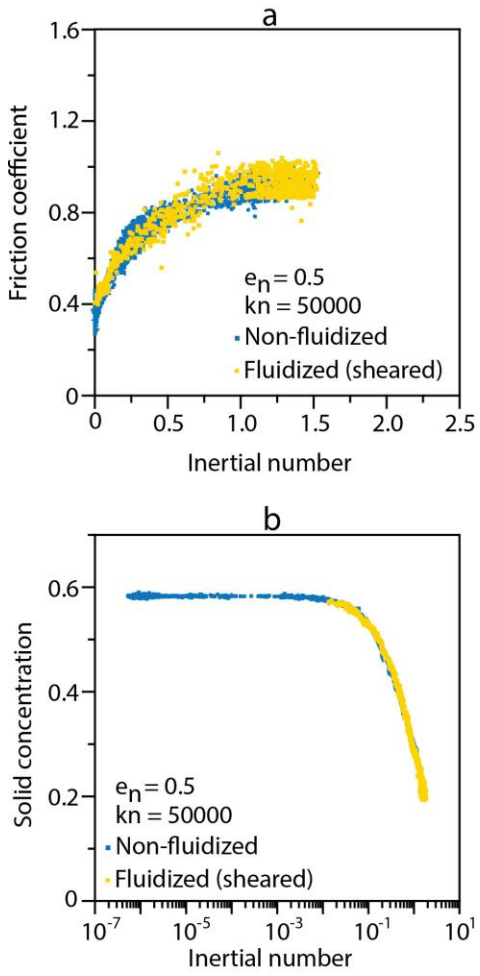

980

981

982 **Fig.5:** Scaling of the friction coefficient (**a**) and solid concentration (**b**) against the inertial number

983 for the sheared non-fluidized and fluidized beds.

984

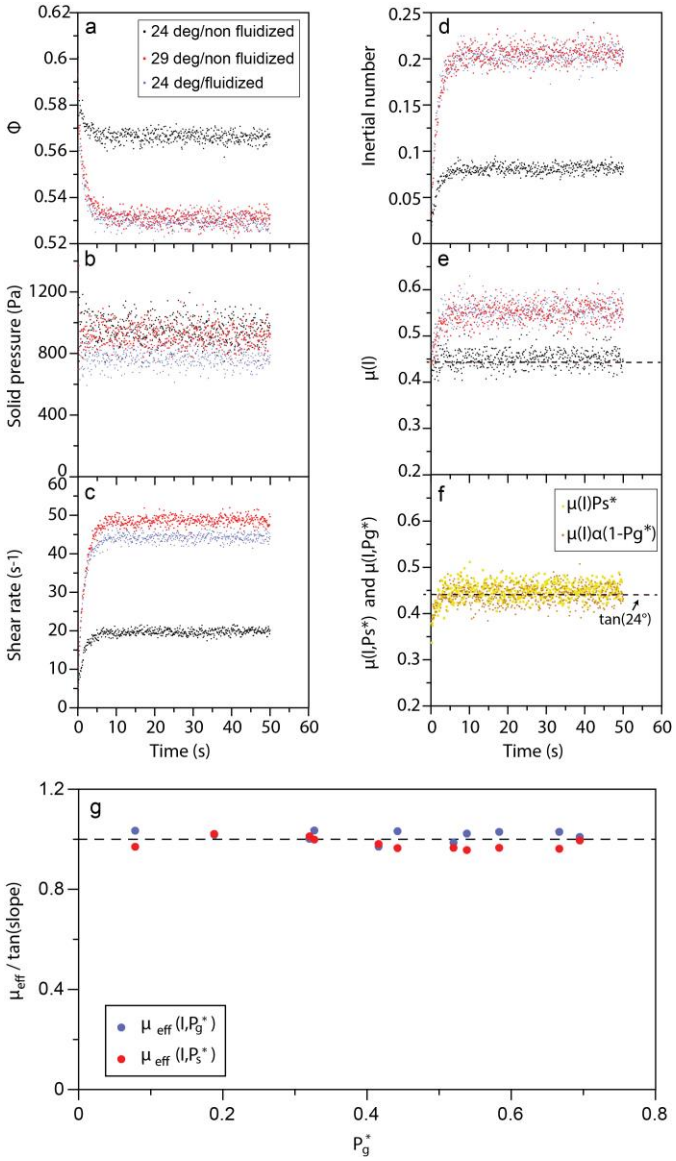

Fig.6: Effective friction coefficient of granular beds with pore pressure. Shear rate (**a**), solid concentration (**b**), non-dimensional pore pressure P_g^* (**c**) and friction data μ(I) (**d**) versus time for a sheared partially fluidized bed on a 24° slope. The gray background illustrates the transient state. In (f), the dashed line represents the tan(slope) = 0.445. In figures **e** and **f**, the friction coefficient μ is corrected and named effective friction coefficient μ_{eff}. In **f**, $\mu_{eff}(I, P_g^*) = \mu(I)(1 - \alpha P_g^*)$ and $\mu_{eff}(I, P_s^*) = \mu(I) P_s^*$. **g**: Plot of μ_{eff}/tan(slope) versus the degree of bed support $=P_g^*$. $Pg^*=0$ when the bed has no excess pore pressure.

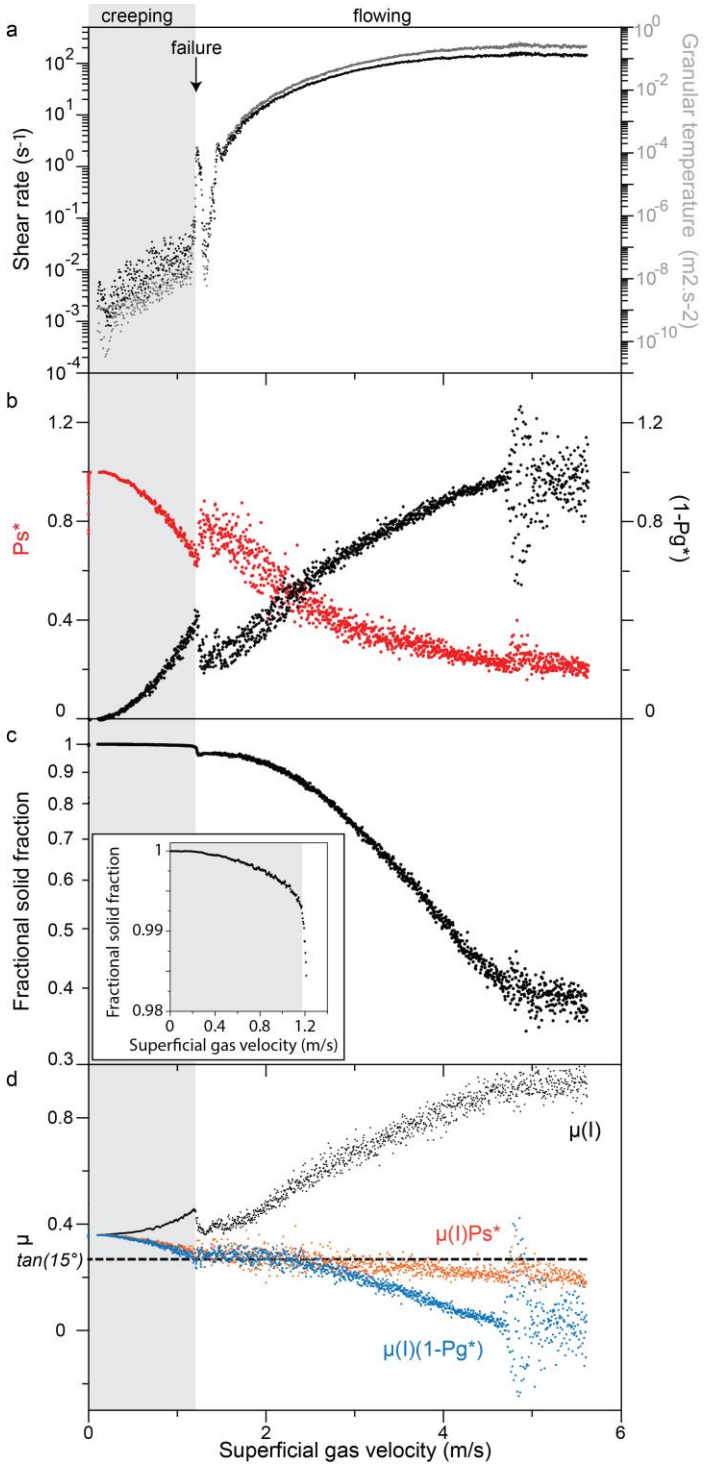

Fig.7: Failure of a progressively fluidized bed on a slope. The figure shows the evolution of the shear rate and granular temperature **(a)**, scaled solid pressure P_s^* and pore pressure $1 - P_g^*$ **(b),** fractional solid concentration (Φ/Φ_{start}) **(c)**, friction coefficients $\mu(I)$, $\mu_{eff}(I, P_s^*)$, $\mu_{eff}(I, P_g^*)$ **(d)** as a function of superficial velocity.

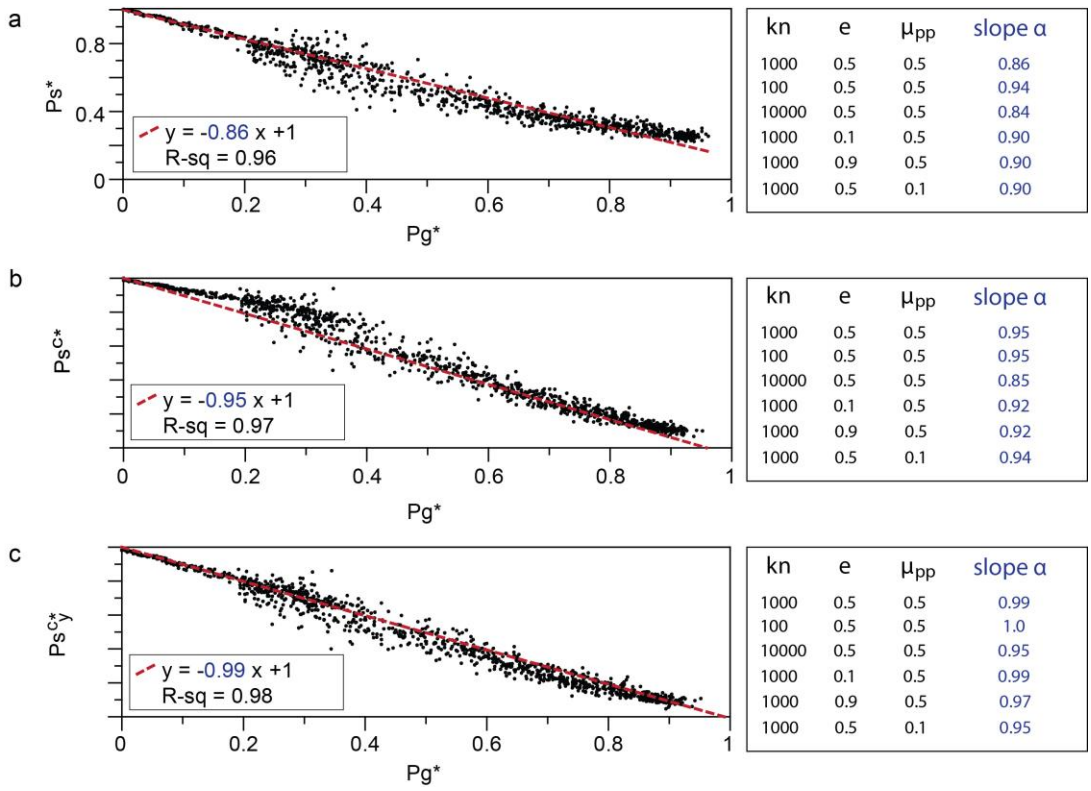

kn	e	μ_{pp}	slope α
1000	0.5	0.5	0.86
100	0.5	0.5	0.94
10000	0.5	0.5	0.84
1000	0.1	0.5	0.90
1000	0.9	0.5	0.90
1000	0.5	0.1	0.90

kn	e	μ_{pp}	slope α
1000	0.5	0.5	0.95
100	0.5	0.5	0.95
10000	0.5	0.5	0.85
1000	0.1	0.5	0.92
1000	0.9	0.5	0.92
1000	0.5	0.1	0.94

kn	e	μ_{pp}	slope α
1000	0.5	0.5	0.99
100	0.5	0.5	1.0
10000	0.5	0.5	0.95
1000	0.1	0.5	0.99
1000	0.9	0.5	0.97
1000	0.5	0.1	0.95

Fig.8: Dimensionless solid pressure P_s^* versus dimensionless gas pore pressure P_g^* (**a**). **b**: Dimensionless solid pressure P_s^{c*} versus P_g^*. P_s^{c*} was calculated from the stress tensor using the collisional contribution only (i.e. excluding the kinetic contribution). In (a) and (b) the pressure is calculated from the 3D components. In (**c**), the pressure $P_s^{c*}{}_y$ was the y component (normal to the substrate) and includes solely the collisional contribution. A linear fit (red dashed line) and its equation is illustrated in each figure. The role of the DEM parameters was investigated running 6 variants of the simulation presented in this figure. We varied independently the spring constant "kn" (unit is Pa.m), the particle restitution coefficient "e" and the particle-particle friction coefficient "μ_{pp}". The slope α of the linear fits are shown for each type of plot (a-c).

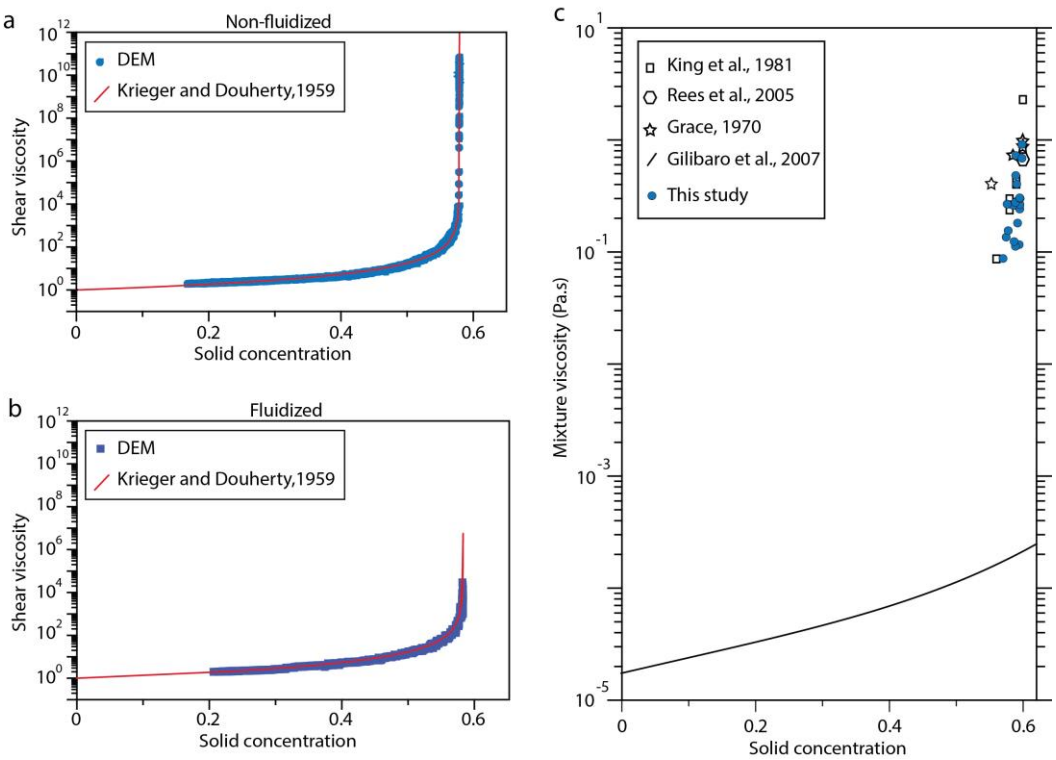

Fig.9: Unifying suspension and granular flow rheologies. **a**: Shear viscosity of the non-fluidized bed with the red line representing the empirical formulation of Krieger and Dougherty (1959). We used a maximum concentration value of 0.583. Eq.34a was used to calculate the DEM-CFD data shown in blue. **b**: Shear viscosity of the fluidized bed with the red line representing the empirical formulation of Krieger and Dougherty (1959). We used a maximum concentration value of 0.583 to fit the Krieger and Dougherty law. Eq.34a was used to calculate the DEM-CFD data shown in blue. **c**: Viscosity of the fluidized bed calculated from Eq.34a from DEM-CFD simulations of 100 microns beads of density equal to 2500 $kg.m^{-3}$ (blue dots), plotted against concentration. Experimental data from (Grace 1970), King et al. (1981) and (Rees et al. 2005) and a theoretical pseudo-fluid prediction from Gibilaro et al. (2007) are also plotted. Note that the viscosity of air is 1.8×10^{-5} Pa.s at 293 K.

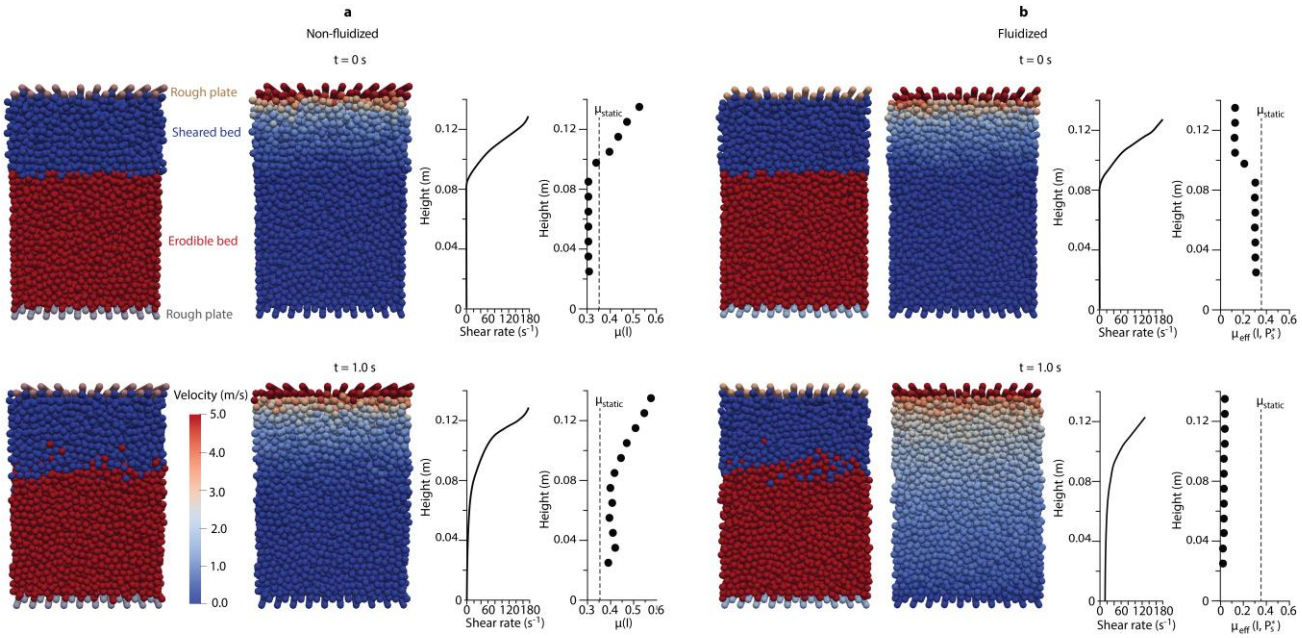

Fig.10: Erosion of the substrate by non-fluidized (**a**) and fluidized beds (**b**) with 5 mm particles. **a**: At t=0s and 1.0s, the shear rate and friction (μ) coefficient are plotted. **b**: At t=0s and 1.0s, the shear rate and effective friction $\mu_{eff}(I, {P_s}^*)$ coefficient is plotted. The particle-particle restitution coefficient and contact stiffness was 0.5 and 10^4 Pa.m, respectively. The particle-particle restitution coefficient and contact stiffness was 0.5 and 10^4 Pa.m, respectively. Particles are colored to represent either their group they belong to (rough top plate with light brown, sheared bed with blue, erodible bed in red and bottom rough plate in gray) or their velocity. The color scale used is the same for all plots. The vertical dotted line represents the static friction coefficient of 0.355.

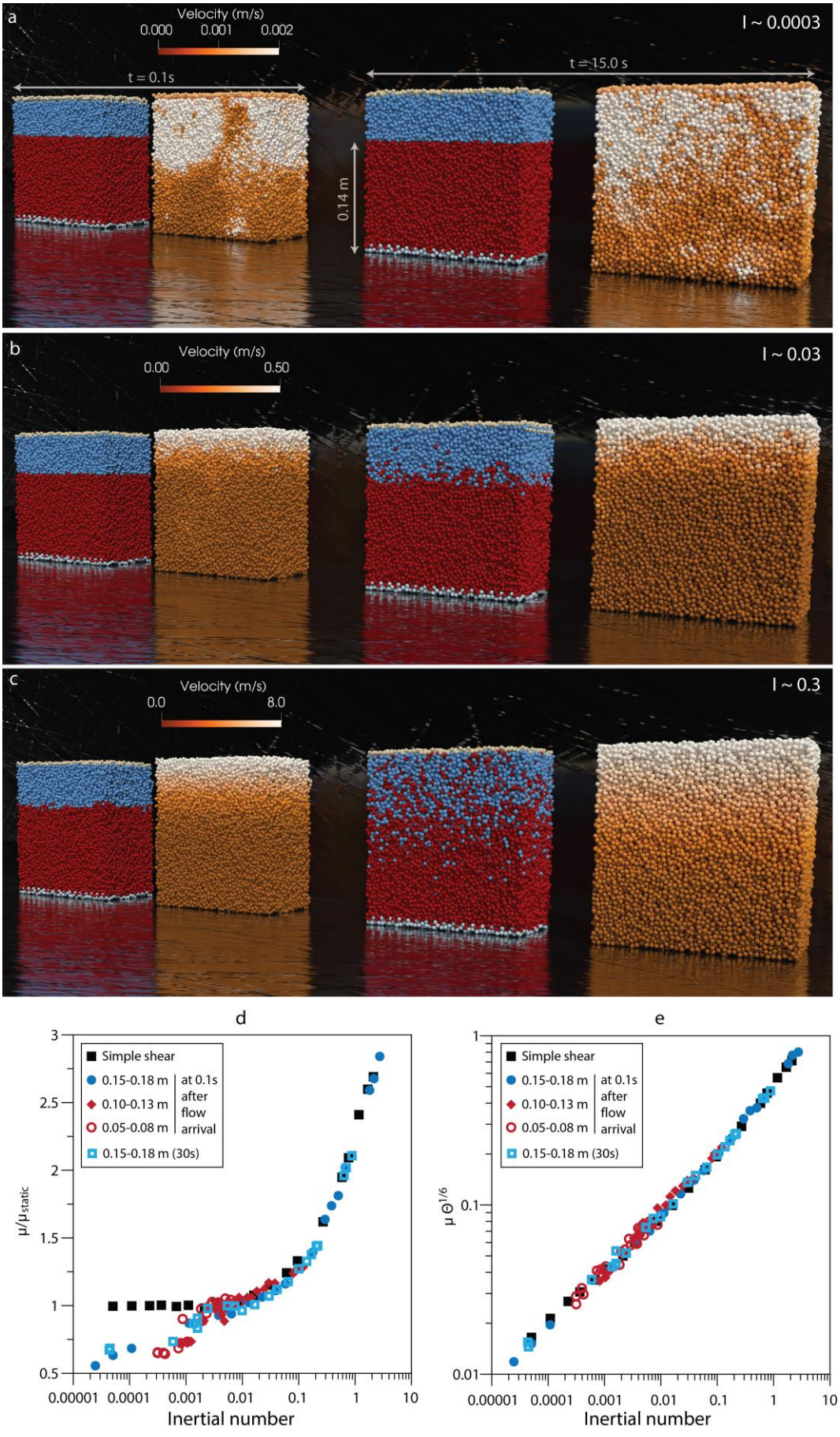
a
Velocity (m/s)
0.000 0.001 0.002
I ~ 0.0003
t = 0.1s
t = 15.0 s
0.14 m
b
Velocity (m/s)
0.00 0.50
I ~ 0.03
c
Velocity (m/s)
0.0 8.0
I ~ 0.3
d
Simple shear
0.15-0.18 m
0.10-0.13 m
0.05-0.08 m
at 0.1s after flow arrival
0.15-0.18 m (30s)
μ/μstatic
Inertial number
e
μ Θ1/6
Inertial number

1037

Fig. 11: Non-local fluidity during propagation of a granular flow over an erodible substrate. A bed in the quasistatic (**a**), intermediate (**b**) and inertial regime (**c**) is shown. The granular flow (blue) and the substrate (red) is made of particles of 5mm±10%. The bed is shown just after arrival of the flow above the substrate for t=0.1s (two beds on left in a, b and c) and at 15s after arrival (two beds on the right). For the 2 timeteps we illustrate the partition of particles in the bottom rough static plate (light blue), erodible substrate (red). Flow (blue) and top rough plate upon which we imposed a constant velocity and confining pressure of 8 kPa. On the right of the red-blue bed we show the velocity of each particles. A set of 23 simulations were ran to span inertial numbers from 10^{-5} to 2. In all simulations gravity was vertical. **d**: plot the dimensionless friction coefficient (μ_{static} is the friction coefficient in simple shear=μ_1 in Eq.2) as a function of the inertial number. The rheology of the flow (simple shear) was measured prior to allowing the substrate to be eroded. Nonlocal fluidity is shown as the dimensionless friction coefficient was lower than 1 in the substrate in the quasistatic and intermediate regime (at t=0.1s and 30s). The data was measured using CG analysis at the height specified (0.15–0.18m). Nonlocal fluidity is rooted in the propagation of velocity fluctuations through particle contacts, and can be quantified through dimensionless granular temperature Θ (Eq.40). **e**: Plot of the friction coefficient corrected using $\Theta^{1/6}$ versus I. The collapse of all data onto a mater curve shows that an increase of granular temperature leads to the lowering of the friction coefficient below the static friction coefficient.

References

Andreotti B, Forterre Y, Pouliquen O (2013) Granular media: between fluid and solid. Cambridge, New York

Aranson IS, Tsimring LS (2002) Continuum theory of partially fluidized granular flows. Phys. Rev. E 65(6):061303

Babic M (1997) Average balance equations for granular materials. International Journal of Engineering Science 35(5):523-548

Bergantz GW, Schleicher JM, Burgisser A (2017) On the kinematics and dynamics of crystal-rich systems. J. Geophys. Res. Solid Earth 122(8):6131-6159

Beverloo WA, Leniger HA, van de Velde J (1961) The flow of granular solids through orifices. Chem. Eng. Sc. 15(3–4):260-269

Biot MA (1962) Mechanics of Deformation and Acoustic Propagation in Porous Media. Journal of Applied Physics 33(4):1482-1498

Bouchut F, Fernández-Nieto ED, Mangeney A, Narbona-Reina G (2016) A two-phase two-layer model for fluidized granular flows with dilatancy effects. J. Fluid. Mech. 801:166-221

Boyer F, Guazzelli É, Pouliquen O (2011) Unifying Suspension and Granular Rheology. Phys. Rev. Lett. 107(18):188301
Branney M, Kokelaar P (2002) Pyroclastic density currents and the sedimentation of ignimbrites. Geological Society Publishing House, Bath, United Kingdom, p 143
Breard ECP, Dufek J, Fullard L, Carrara A (2020) The Basal Friction Coefficient of Granular Flows With and Without Excess Pore Pressure: Implications for Pyroclastic Density Currents, Water-Rich Debris Flows, and Rock and Submarine Avalanches. J. Geophys. Res. Solid Earth 125(12):e2020JB020203
Breard ECP, Dufek J, Lube G (2017) Enhanced Mobility in Concentrated Pyroclastic Density Currents: An Examination of a Self-Fluidization Mechanism. Geophys. R. Lett. 45:654–664
Breard ECP, Dufek J, Roche O (2019) Continuum Modeling of Pressure-Balanced and Fluidized Granular Flows in 2-D: Comparison With Glass Bead Experiments and Implications for Concentrated Pyroclastic Density Currents. J. Geophys. Res. Solid Earth 124(6):5557-5583
Breard ECP, Jones JR, Fullard L, Lube G, Davies C, Dufek J (2019) The permeability of volcanic mixtures—implications for pyroclastic currents. J. Geophys. Res. Solid Earth 124(2):1343-1360
Brown MC (1962) Nuees ardentes and fluidization. American Journal of Science 260(6):467-470
Calder ES, Sparks RSJ, Gardeweg MC (2000) Erosion, transport and segregation of pumice and lithic clasts in pyroclastic flows inferred from ignimbrite at Lascar Volcano, Chile. J. Volcanol. Geotherm. Res. 104(1-4):201-235
Capra L, Manea VC, Manea M, Norini G (2011) The importance of digital elevation model resolution on granular flow simulations; a test case for Colima Volcano using TITAN2D computational routine. Natural Hazards 59(2):665-680
Carrara A, Burgisser A, Bergantz GW (2019) Lubrication effects on magmatic mush dynamics. J. Volcanol. Geotherm. Res. 380:19-30
Charbonnier SJ, Germa A, Connor CB, Gertisser R, Preece K, Komorowski J-C, Lavigne F, Dixon T, Connor L (2013) Evaluation of the impact of the 2010 pyroclastic density currents at Merapi Volcano from high-resolution satellite imagery, field investigations and numerical simulations. J. Volcanol. Geotherm. Res. 261:295-315
Charbonnier SJ, Gertisser R (2009) Numerical simulations of block-and-ash flows using the Titan2D flow model; examples from the 2006 eruption of Merapi Volcano, Java, Indonesia. Bull. Volcanol. 71(8):953-959
Chen JC, Grace JR, Golriz MR (2005) Heat transfer in fluidized beds: design methods. Powder Technology 150(2):123-132
Chialvo S, Sun J, Sundaresan S (2012) Bridging the rheology of granular flows in three regimes. Phys. Rev. E 85(2):021305
Chialvo S, Sundaresan S (2013) A modified kinetic theory for frictional granular flows in dense and dilute regimes. Phys. Fluid 25(7):070603
Cleary PW, Sawley ML (2002) DEM modelling of industrial granular flows: 3D case studies and the effect of particle shape on hopper discharge. Applied Mathematical Modelling 26(2):89-111
Coulomb CA (1781) “Theorie des Machines Simples.”. Academie des Sciences 166(10)
da Cruz F, Emam S, Prochnow M, Roux J.-N., Chevoir F (2005) Rheophysics of dense granular materials: Discrete simulation of plane shear flows. Phys. Rev. E (72):021309
de' Michieli Vitturi M, Esposti Ongaro T, Lari G, Aravena A (2019) IMEX_SfloW2D 1.0: a depth-averaged numerical flow model for pyroclastic avalanches. Geosci. Model Dev. 12(1):581-595
Druitt TH, Avard G, Bruni G, Lettieri P, Maez F (2007) Gas retention in fine-grained pyroclastic flow materials at high temperatures. Bull. Volcanol. 69(8):881-901
Druitt TH, Bruni G, Lettieri P, Yates JG (2004) The fluidization behaviour of ignimbrite at high temperature and with mechanical agitation. Geophys. R. Lett. 31(2)

Druitt TH, Calder ES, Cole PD, Hoblitt RP, Loughlin SC, Norton GE, Ritchie LJ, Sparks RSJ, Voight B (2002) Small-volume, highly mobile pyroclastic flows formed by rapid sedimentation from pyroclastic surges at Soufriere Hills Volcano, Montserrat; an important volcanic hazard. Mem. Geol. Soc. London 21:263-279
Edwards AN, Gray JMNT (2014) Erosion–deposition waves in shallow granular free-surface flows. J. Fluid. Mech. 762:35-67
Einstein A (1905) Über die von der molekularkinetischen Theorie der Wärme geforderte Bewegung von in ruhenden Flüssigkeiten suspendierten Teilchen. Annalen der Physik 322(8):549-560
Fall A, Ovarlez G, Hautemayou D, Mézière C, Roux JN, Chevoir F (2015) Dry granular flows: Rheological measurements of the μ(I)-rheology. Journal of Rheology 59(4):1065-1080
Forterre Y, Pouliquen O (2008) Flows of Dense Granular Media. Annu. Rev. Fluid Mech. 40(1):1-24
Freundt A (1998) The formation of high-grade ignimbrites, I: Experiments on high- and low-concentration transport systems containing sticky particles. Bull. Volcanol. 59(6):414-435
Fullard L, Breard E, Davies C, Lagrée P-Y, Popinet S, Lube G (2017) Testing the μ(I) granular rheology against experimental silo data. EPJ Web Conf. 140:11002
Gallier S, Lemaire E, Peters F, Lobry L (2014) Rheology of sheared suspensions of rough frictional particles. J. Fluid. Mech. 757:514-549
Garg R, Galvin J, Li T, Pannala S (2012) Open-source MFIX-DEM software for gas–solids flows: Part I—Verification studies. Powder Technology 220:122-137
Gauer P, Issler D (2017) Possible erosion mechanisms in snow avalanches. Annals of Glaciology 38:384-392
GDR-MiDi (2004) Eur. Phys. J. E 14, 341.
Geldart D (1973) Types of gas fluidization. Powder Technology 7(5):285-292
Gibilaro LG, Gallucci K, Di Felice R, Pagliai P (2007) On the apparent viscosity of a fluidized bed. Chem. Eng. Sc. 62(1–2):294-300
Girolami L, Druitt TH, Roche O (2007) Dynamics of laboratory ash flows. International Union of Geodesy and Geophysics General Assembly = Union Geodesique et Geophysique Internationale Comptes Rendus de la ...Assemblee Generale 24
Grace JR (1970) The viscosity of fluidized beds. The Canadian Journal of Chemical Engineering 48(1):30-33
Grace JR (1992) Agricola aground: Characterization and interpretation of fluidization phenomena. AIChE Symposium Series 289 (88):1-16
Gu Y, Ozel A, Sundaresan S (2016) Rheology of granular materials with size distributions across dense-flow regimes. Powder Technology 295(Supplement C):322-329
Gueugneau V, Kelfoun K, Charbonnier S, Germa A, Carazzo G (2020) Dynamics and Impacts of the May 8th, 1902 Pyroclastic Current at Mount Pelée (Martinique): New Insights From Numerical Modeling. Front. Earth Sci. 8(279)
Gueugneau V, Kelfoun K, Roche O, Chupin L (2017) Effects of pore pressure in pyroclastic flows: Numerical simulation and experimental validation. Geophys. R. Lett. 44(5):2194-2202
Guo N, Zhao J (2013) The signature of shear-induced anisotropy in granular media. Computers and Geotechnics 47:1-15
Hartkamp R, Ghosh A, Weinhart T, Luding S (2012) A study of the anisotropy of stress in a fluid confined in a nanochannel. The Journal of Chemical Physics 137(4):044711
Henann DL, Kamrin K (2013) A predictive, size-dependent continuum model for dense granular flows. Proc. Natl Acad. Sci. 110(17):6730
Holyoake AJ, McElwaine JN (2012) High-speed granular chute flows. J. Fluid. Mech. 710:35-71
Hutter K (2005) Geophysical granular and particle-laden flows: review of the field. Philosophical Transactions of the Royal Society A: Mathematical, Physical and Engineering Sciences 363(1832):1497

Iverson RH (1997) The physics of debris flows. Rev. Geophys. 35(3):245-296
Iverson RM (2005) Regulation of landslide motion by dilatancy and pore pressure feedback. J. Geophys. Res. Earth Surface 110(F2):n/a-n/a
Iverson RM, George DL (2014) A depth-averaged debris-flow model that includes the effects of evolving dilatancy. I. Physical basis. Proceedings of the Royal Society A: Mathematical, Physical and Engineering Sciences 470(2170):20130819
Iverson RM, Lahusen RG (1989) Dynamic pore-pressure fluctuations in rapidly shearing granular materials. Science 246(4831)
Iverson RM, Logan M, LaHusen RG, Berti M (2010) The perfect debris flow? Aggregated results from 28 large-scale experiments. J. Geophys. Res. Earth Surface 115(F3)
Iverson RM, Reid ME, LaHusen RG (1997) Debris-flow mobilization from landslides. Annu. Rev. Earth Planet. Sci. 25(1):85-138
Iverson RM, Reid ME, Logan M, LaHusen RG, Godt JW, Griswold JP (2010) Positive feedback and momentum growth during debris-flow entrainment of wet bed sediment. Nat. Geosci. 4:116
Iverson RM, Vallance JW (2001) New views of granular mass flows. Geology 29(2):115-118
Jaeger HM, Nagel SR (1992) Physics of the Granular State. Science 255(5051):1523
Janda A, Zuriguel I, Garcimartín A, Maza D (2015) Clogging of granular materials in narrow vertical pipes discharged at constant velocity. Granular Matter 17(5):545-551
Jessop DE, Hogg AJ, Gilbertson MA, Schoof C (2017) Steady and unsteady fluidised granular flows down slopes. J. Fluid. Mech. 827:67-120
Jop P, Forterre Y, Pouliquen O (2005) Crucial role of sidewalls in granular surface flows: consequences for the rheology. J. Fluid. Mech. 541:167-192
Jop P, Forterre Y, Pouliquen O (2006) A constitutive law for dense granular flows. Nature (441):727-730
Kamrin K, Henann DL (2015) Nonlocal modeling of granular flows down inclines. Soft Matter 11:179-185
Kamrin K, Koval G (2012) Nonlocal Constitutive Relation for Steady Granular Flow. Phys. Rev. Lett. 108(17):178301
Kelfoun K (2011) Suitability of simple rheological laws for the numerical simulation of dense pyroclastic flows and long-runout volcanic avalanches. J. Geophys. Res. 116(B8)
Kelfoun K (2017) A two-layer depth-averaged model for both the dilute and the concentrated parts of pyroclastic currents. J. Geophys. Res. Solid Earth 122(6):4293-4311
Kim S, Kamrin K (2020) Power-Law Scaling in Granular Rheology across Flow Geometries. Phys. Rev. Lett. 125(8):088002
King DF, Mitchell FRG, Harrison D (1981) Dense phase viscosities of fluidised beds at elevated pressures. Powder Technology 28(1):55-58
Krieger IM, Dougherty TJ (1959) A Mechanism for Non-Newtonian Flow in Suspensions of Rigid Spheres. Transactions of the Society of Rheology 3(1):137-152
Kunii D, Levespiel O (1991) Fluidization Engineering 2nd edition. Butterworth-Heinemann
Langston PA, Tüzün U, Heyes DM (1995) Discrete element simulation of granular flow in 2D and 3D hoppers: Dependence of discharge rate and wall stress on particle interactions. Chem. Eng. Sc. 50(6):967-987
Li T, Garg R, Galvin J, Pannala S (2012) Open-source MFIX-DEM software for gas-solids flows: Part II — Validation studies. Powder Technology 220(Supplement C):138-150
Lube G, Breard ECP, Esposti-Ongaro T, Dufek J, Brand B (2020) Multiphase flow behaviour and hazard prediction of pyroclastic density currents. Nature Reviews Earth & Environment 1(7):348-365
Lube G, Breard ECP, Jones J, Fullard L, Dufek J, Cronin SJ, Wang T (2019) Generation of air lubrication within pyroclastic density currents. Nat. Geosci. 12(5):381-386

Lucas A, Mangeney A, Ampuero JP (2014) Frictional velocity-weakening in landslides on Earth and on other planetary bodies. Nat. Commun. 5(1):3417
Lun CKK, Savage SB, Jeffrey DJ, Chepurniy N (1984) Kinetic theories for granular flow: inelastic particles in Couette flow and slightly inelastic particles in a general flowfield. J. Fluid. Mech. 140:223-256
Marzougui D, Chareyre B, Chauchat J (2015) Microscopic origins of shear stress in dense fluid–grain mixtures. Granular Matter 17(3):297-309
Mickley HS, Fairbanks DF (1955) Mechanism of heat transfer to fluidized beds. AIChE Journal 1(3):374-384
Montserrat S, Tamburrino A, Roche O, Niño Y (2012) Pore fluid pressure diffusion in defluidizing granular columns. J. Geophys. Res. Earth Surface 117(F2)
Musser J, Vaidheeswaran A, Clarke MA (2021) MFIX Documentation Volume 3: Verification and Validation Manual; 3rd ed. NETL-PUB-22050; NETL Technical Report Series; U.S. Department of Energy, National Energy Technology Laboratory: Morgantown, WV.
Ness C, Sun J (2015) Flow regime transitions in dense non-Brownian suspensions: Rheology, microstructural characterization, and constitutive modeling. Phys. Rev. E 91(1):012201
Ogburn SE, Calder ES (2017) The Relative Effectiveness of Empirical and Physical Models for Simulating the Dense Undercurrent of Pyroclastic Flows under Different Emplacement Conditions. Front. Earth Sci. 5(83)
Pailha M, Nicolas M, Pouliquen O (2008) Initiation of underwater granular avalanches: Influence of the initial volume fraction. Phys. Fluid 20(11):111701
Pouliquen O, Vallance JW (1999) Segregation induced instabilities of granular fronts. Chaos 3(9):621-630
Queteschiner D, Lichtenegger T, Schneiderbauer S, Pirker S (2017) Adaptive coarse-graining for large-scale DEM simulations. In: 12th International Conference on CFD in Oil & Gas, Metallurgical and Process Industries. Norway
Rees AC, Davidson JF, Dennis JS, Hayhurst AN (2005) The rise of a buoyant sphere in a gas-fluidized bed. Chem. Eng. Sc. 60(4):1143-1153
Reynolds O (1885) On the dilatancy of media composed of rigid particles in contact. Philos. 1550 Mag. Ser. 5, 50-20, 469.
Roche O (2012) Depositional processes and gas pore pressure in pyroclastic flows: an experimental perspective. Bull. Volcanol. 74(8):1807-1820
Roche O, Buesch DC, Valentine GA (2016) Slow-moving and far-travelled dense pyroclastic flows during the Peach Spring super-eruption. Nat Commun 7
Roche O, Gilbertson MA, Phillips JC, Sparks RSJ (2005) Inviscid behaviour of fines-rich pyroclastic flows inferred from experiments on gas–particle mixtures. Earth Planet. Sci. Lett. 240(2):401-414
Roche O, Nino Y, Mangeney A, Brand B, Pollock N, Valentine GA (2013) Dynamic pore-pressure variations induce substrate erosion by pyroclastic flows. Geology 41(10):1107-1110
Roux R, Radjai F (1998) in Physics of dry granular media. Springer, pp 229–236
Rubio-Largo SM, Janda A, Maza D, Zuriguel I, Hidalgo RC (2015) Disentangling the free-fall arch paradox in silo discharge. Phys. Rev. Lett.
Schoefield A, Wroth P (1968) Critical State Soil Mechanics. McGraw-Hill,
Smith GM, Williams R, Rowley PJ, Parsons DR (2018) Investigation of variable aeration of monodisperse mixtures: implications for pyroclastic density currents. Bull. Volcanol. 80(8):67
Sparks RSJ (1976) Grain size variations in ignimbrites and implications for the transport of pyroclastic flows. Sedimentology 23(2):147-188
Stickel JJ, Powell RL (2005) FLUID MECHANICS AND RHEOLOGY OF DENSE SUSPENSIONS. Annu. Rev. Fluid Mech. 37(1):129-149

Sutherland W, (1893), (1893) The viscosity of gases and molecular force Philosophical Magazine, S. 5, 36:507-531
Terzaghi K (1936) The shearing resistance of saturated soils and the angle between the planes of shear. Proceedings of the first international conference on soil mechanics and foundation engineering, D-7.
Thornton A, Weinhart T, Luding S, Bokhove O (2012) Modeling of the particle size segregation: calibration using the discrete particle method. International Journal of Modern Physics C 23(08):1240014
Weinhart T, Hartkamp R, Thornton AR, Luding S (2013) Coarse-grained local and objective continuum description of three-dimensional granular flows down an inclined surface. Phys. Fluid 25(7):070605
Weinhart T, Labra C, Luding S, Ooi JY (2016) Influence of coarse-graining parameters on the analysis of DEM simulations of silo flow. Powder Technology 293:138-148
Weinhart T, Thornton AR, Luding S, Bokhove O (2012) Closure relations for shallow granular flows from particle simulations. Granular Matter 14(4):531-552
Wilson CJN (1980) The role of fluidization in the emplacement of pyroclastic flows: an experimental approach. J. Volcanol. Geotherm. Res. 8:231-249
Wilson CJN (1984) The role of fluidization in the emplacement of pyroclastic flows, 2: Experimental results and their interpretation. J. Volcanol. Geotherm. Res. 20(1):55-84
Wood DM (1990) Soil behaviour and critical state soil mechanics. Cambridge university press,
Wood DM (1991) Introduction: models and soil mechanics. In: Wood DM (ed) Soil Behaviour and Critical State Soil Mechanics. Cambridge University Press, Cambridge, pp 1-36
Yang M, Taiebat M, Mutabaruka P, Radjaï F (2021) Evolution of granular materials under isochoric cyclic simple shearing. Phys. Rev. E 103(3):032904
Zhang Q, Kamrin K (2017) Microscopic Description of the Granular Fluidity Field in Nonlocal Flow Modeling. Phys. Rev. Lett. 118(5):058001